Supercell storms in Switzerland: Case studies and implications for now-casting severe winds with Doppler radar

Running title: **Supercell storms in Switzerland**

W. Schmid[1], H.-H. Schiesser[1], and B. Bauer-Messmer[2]

[1]Institute for Atmospheric Science, ETH, CH-8093 Zurich (Switzerland)

[2]Water Resources Program, Department of Civil Engineering,

Princeton University, NJ 80544 (U.S.A.)

Final manuscript, published in ***Meteorol. Appl. 4, 49-67 (1997)***

Corresponding author: *Dr. W. Schmid*
Atmospheric Science, ETH
CH-8093 Zürich, Switzerland
Phone: +41 1 633 36 25
Fax: +41 1 633 10 58
Email: schmid@atmos.umnw.ethz.ch

Abstract

Three severe hail- and windstorms, which occurred in Northern Switzerland, have been investigated. The storms produced hailswaths of 70-170 km in length and 12-25 km in width. Compact tracks of severe wind damages within the hailswaths are documented from public reports. These tracks have a length of 12-25 km. The damages were produced by straight-line winds rather than by tornadoes. Volume-scan Doppler radar data of the storms are available in time steps of 5 min. Radar signatures, such as low-level convergence and shear, mid-level vorticity, and high-level divergence, were attributed to the damage tracks at the ground. The low-level radar signatures allow to deduce the time of occurrence of the damage tracks with a precision of some minutes.

Striking similarities in the evolution of the three storms were found. The storms developed in the foothills of the Alps and the Jura mountains and propagated towards the plains of the Swiss midland. The storms can be classified as “high-precipitation” supercell storms, known as producers of severe straight-line winds in the U.S. Meso(anti)cyclonic vortex signatures were seen 40-55 min in advance of the heavy wind damages at the ground. The damage tracks were associated with explosive secondary cellular growth aloft. The physical explanation of this behaviour is that the first cells with mid-level rotation produced a gust front outflow that was accelerated to damaging strength at the time when the secondary cellular growth was initiated. The operational implication is that the nowcasting of severe and damaging winds can be improved considering mid-level rotation in an early stage of the evolving storms.

1. Introduction

Severe thunderstorms associated with hail and wind gusts can cause damages to extended areas. Major hailswaths reach some 100 km in length and some 10 km in width (e.g., Changnon, 1970), but damaging wind gusts (e.g., downbursts or tornadoes) occur on a smaller scale. Aisles of broken trees and damaged buildings due to strong winds reach some 10 km in length and some 100 m to a few kilometers in width. Strong wind may exacerbate the damage due to hail alone and, as a consequence, may also increase the danger to human life. This is especially true for a densely populated area. Warnings of severe wind gusts can help citizens to take care of exposed trees and buildings and to reach protected zones in time.

In this study, three severe storms are investigated that occurred in Northern Switzerland during 1992. The storms produced hailswaths of 70-170 km in length and 12-25 km in width. Hereafter, we will concentrate on the wind damage that was associated with these storms. Compact tracks of severe wind damage in the forests and populated areas are documented from public reports. The damage was caused by non-tornadic wind events. Volumetric Doppler radar data of the storms were collected within the framework of a National Research Program (NRP31, “climate changes and natural disasters”). The radar data, together with additional data (satellite data, radiosoundings, ground mesonetwork), allow the documentation of the evolution of the storms from their origin until when the severe wind damage occurred. The data base from these storms yields a unique opportunity to explore various criteria for nowcasting the strong wind events associated with these storms. This is the main purpose of this study.

The three storms were supercellular. Supercell storms are a unique class of convective storms, characterized by a long life (up to several hours), a motion that deviates from the mean winds, and specific radar features. Early conceptual models of supercell storms were developed on the basis of non-Doppler radar data and include features like a “vault” or “weak echo region” (Browning & Ludlam, 1962; Browning, 1977), a “hook” (Lemon & Doswell, 1979), or a continuous and “steady-state” propagation (Browning, 1964). Doppler radar observations showed that the weak echo region is associated with vortex signatures, indicating substantial rotation of the airmass at midlevels (Donaldson, 1970). Based on numerous modelling studies, it is now generally accepted that *rotating updrafts* play a vital role in producing the specific storm motion and the radar features of supercell storms (Rotunno, 1993). The research on supercell storms has a long tradition in the U.S. (e.g., Rotunno, 1993; Moller et al., 1994) whereas, in Europe, much less scientific work on supercell storms is available, in spite of the pioneering studies by Browning & Ludlam (1962) and Browning (1964). The main reason for

this diverging interest might be that supercell storms in central U.S often spawn violent tornadoes. In Europe, tornadoes are less frequently observed (Dessens & Snow, 1993), and few studies are available that associate European tornadoes with supercell storms (e.g., Alberoni et al., 1996). This may mean that European supercell storms are typically non-tornadic, or it may mean that supercell storms in Europe are rare events compared to central U.S. Climatological data on the frequency of occurrence of European supercell storms only exist for specific regions. Historical radar data from the "Grossversuch IV" hail suppression project (1975-1982) in Central Switzerland, for instance, revealed 18 severe hailstorms with a hook structure typical of supercell storms (Houze et al., 1993). Thus, about two or three supercell storms may occur each year in Central Switzerland. This finding is in a good agreement with recent Doppler radar observations. A sample of eight supercell storms was documented in Eastern Switzerland during 1992-1994 (Schmid et al., 1996). None of these storms were accompanied by visual observations of tornadoes. Rather, the storms produced severe hail damage, and part of each storm was associated with severe straight-line (i.e. non-tornadic) winds. The storms analysed here are part of this storm sample and therefore represent an important type of severe and damaging thunderstorm.

First, we will document the damage data and the associated radar patterns measured at low altitudes. In a second step, we will summarize the meteorological environment in which the storms developed. After that, the radar history of the storms is investigated from an early stage of their evolution until when the severe wind damage occurred. We will show that the supercellular stage is reached well in advance of the occurrence of the wind damage. The combination of the damage and radar data allows insight into the possible mechanisms that led to the formation of the damaging wind gusts. At the end, a comparison of the analysed storms with the supercell spectrum seen in the U.S. is made, and the implications for operational nowcasting of such storms are summarized.

2. Data and procedures

2.1. The radars

Three radars are used in this study. The positions of the radars, together with other measuring devices, are given in Figure 1. Two non-Doppler C-band radars, operated by the Swiss Meteorological Institute (SMI hereafter; all abbreviations and symbols are defined and explained in the Appendix), are used to monitor the evolution of thunderstorms over a large area (500x400 km). More detailed studies are possible with the C-band Doppler weather radar of the ETH in Zurich. This radar is in operation since 1990. The characteristics of the radar and the measuring program for thunderstorm situations are given in Table 1. The IRIS-software, developed by Sigmet Inc., is used for the radar operations, for storage of the radar data and for creation of various types of radar products. More details on the radar can be found in Li et al. (1995).

The radar allows the collection of PPIs, RHIs and sector-volume scans of the most severe thunderstorms. PPIs are radar scans at a constant elevation angle about a horizontal plane whereas, for a RHI, the radar scans in a vertical plane at a constant azimuth angle. The volume of a thunderstorm can be scanned by moving the radar antenna several times in the PPI mode between two azimuth angles, each time with another elevation angle. Such a scanning mode is called a “sector-volume” scan. The ranges in azimuth, distance and altitude of the volumes to be scanned are entered interactively by the radar operator. The number and the elevation angles of the scans are computed automatically in such a way that a sector-volume scan lasts less than 2 min. The number of scans is 15 for narrow sectors (30-45^{o}) but may decrease to 9 or less for sectors that are broader than 90^{o}. This means that the resolution in altitude is excellent (1-1.5 km) for storms that are in a medium distance from the radar (40-80 km). The storms are captured with a coarser resolution when they are close to the radar. Normally, sector-volume scans are only made when the storms are within 80-100 km of the radar.

The aim of the sector-volume scans is to obtain complete measuring sequences of developing storms. The scans are repeated every 5 min with a series of RHIs (typically 3-11) between each sector-volume scan. The RHIs are helpful in the detection of low-level convergence and high-level divergence. We add two 360^{o} PPI-scans (typically at 1.5^{o} and 20^{o} elevation) every 10 min in order to get an overview of thunderstorm evolution in the radar range. Profiles of horizontal wind at the location of the radar can be computed from the PPI data by using a mod-

ified VAD-technique (“velocity-azimuth display”, see Waldteufel & Corbin, 1979 and Siggia, 1991).

Operational radar systems allow not only a sector-volume but a full-volume scan to be obtained with a time resolution of 5 min (Joss & Lee, 1995). This means that a large amount of data can be collected for all storms within the radar range without the need to identify an appropriate sector-volume. The spatial resolution of full-volume scans, however, does not necessarily reach the spatial resolution of sector-volume scans. Further studies have to show whether the investigated parameters and proposed criteria can be determined with sufficient accuracy when using data from operational weather radar systems.

2.2. Radar quantities

This section describes signatures and parameters that are related to the strength, severity and internal structure of a thunderstorm: the maximum altitude of the 45 dBZ volume (H_{45}), the altitude, size, duration and strength of vortex signatures and mesocyclones, and signatures of high-level divergence. In the following subsections, we present some examples, in order to illustrate the procedures that are used to obtain the relevant quantities.

(a) Criteria based on radar reflectivity

Reflectivities larger than 55 dBZ are often attributed to hail (e.g., Geotis, 1963 or Waldvogel et al., 1978). A number of criteria based on radar reflectivity has been defined to characterize the “strength” of a convective storm (e.g., the radar-derived hail kinetic energy, or the “vertically-integrated liquid water content”). We refer to Joss & Waldvogel (1990) for an overview on the various criteria. Here, we select H_{45} as a good indicator for the strength of a hail cell (Waldvogel et al., 1979) where H_{45} is the maximum altitude of the volume filled with reflectivities $\geq$ 45 dBZ. This criterion has the advantage that it is relatively insensitive to attenuation effects when using a C-band radar since it is measured at high altitudes, i.e. in a range where non-attenuating ice particles dominate.

Another possible way of identifying severe storms is to look at specific features in the reflectivity pattern. Echo indentations or “holes” in the radar patterns at low levels (typically 1-5 km) are often superimposed by high-intensity echoes at higher levels. Such features, often denoted as “hook echoes”, “vaults”, “weak echo regions”, or “bounded weak echo regions” indicate rotating updrafts and supercell storms (see e.g., Burgess & Lemon, 1990). Operational ap-

plication of such criteria for detection of supercell storms is somewhat ambiguous when using C-band radar data. The described features might be artefacts, caused by attenuation at low levels. Hereafter, we will not consider the shape of the radar echoes. We only mention that “weak echo regions” have been observed in all three storms discussed hereafter.

(b) Low-level convergence and high-level divergence

Additional criteria for severe storms can be defined and investigated with Doppler radar (see e.g., Burgess & Lemon, 1990). Important criteria are the convergence near the ground and the divergence near cloud tops. A measure of the strength of these patterns is the parameter DV, defined as the difference between the two extremes in Doppler velocity that are attributed to the signature. Hereafter, positive (negative) values for this parameter refer to divergent (convergent) patterns. Low-level convergence is often invisible for several reasons (missing radar targets, attenuation, or clutter and shielding effects). Therefore, it is preferable to consider high-level divergence for severe storm detection. Witt & Nelson (1991) found a good correlation between DV measured aloft and the maximum size of hailstones collected at the ground. Maximum hailstone diameters may reach 2.5 (5) cm for DV ~ 40 (80) m s^{-1}.

Low-level convergence and high-level divergence can be seen in RHI- and PPI-sections as well. RHI-sections can provide a high probability of detection of these signatures. Examples of low-level convergence and high-level divergence are shown in the RHI-sections in Figures 2(b) and 3(b). The value of DV near cloud top is 50 m s^{-1} in the example shown in Figure 2(b) but 80 m s^{-1} is reached in a neighbouring RHI-section (not shown here). Values of 150 m s^{-1} for DV are occasionally observed in Oklahoma (Witt & Nelson, 1991).

(c) Vortex signatures and mesocyclones

Rotation in thunderstorms on the scale of some kilometers can be seen with a Doppler radar. Doppler signatures of such rotation are precursors of tornadoes which explains the attention of U.S. scientists to thunderstorm rotation over the last few decades (e.g., Church et al., 1993). An overview on the detection of thunderstorm rotation with a Doppler radar is given by Burgess & Lemon (1990). Here, we adopt the existing definition of a vortex signature (VS hereafter) with minor modifications. A VS is attributed to the core region of a vortex that is characterized by a pair of maximum and minimum in the Doppler velocity, located at the same distance from the radar (e.g., Donaldson, 1970). Figure 2(a) indicates an anticyclonic VS. It may happen that the line through the neighbouring extremes of Doppler velocity is rotated by some angle from the

azimuthal direction, indicating that the signature is associated with convergence or divergence (e.g., Brown & Wood, 1991). Such signatures are accepted as VSs as long as the deviating angle is less than 30^o. An example of such a VS, associated with some convergence, is shown in Figure 3(a).

Important parameters characterizing a VS are the distance (D, in km), the difference (ΔV, in m s^{-1}) and the shear ($\Delta V/D$, in s^{-1}) between the extremes in Doppler velocity. The quantity $\Delta V/2$ is also referred to as "rotational velocity" (e.g., Burgess & Lemon, 1990). Additional parameters are the mean altitude (h, in km MSL) at which the VS is observed, and the vertical extent (Δh, in km) of a VS. Here, the VSs and related parameters are identified by scanning through all available sector-volume scans of the storms, using the following guidelines:

- A *mesocyclonic VS* (*MVS* hereafter) fulfils the conditions $\Delta V > 26$ m s^{-1} and $\Delta V/D > 0.005$ s^{-1}. The shear criterion weakens to $\Delta V/D > 0.025$ s^{-1} if $\Delta V > 32$ m s^{-1}. This considers the fact that a large (D ~ 12 km) VS does not necessarily reach a shear of 0.005 s^{-1} (see the example shown in Figure 3(a)).
- A *mesocyclone* is a MVS that reaches a vertical extent $\Delta h > 4$ km for at least 30 min.

These criteria for a mesocyclone are adopted from U.S. definitions (e.g., Moller et al., 1994). Meso*anti*cyclonic VSs (also called MVS hereafter) and meso*anti*cyclones fulfil the same criteria as mesocyclonic VSs and mesocyclones, with the exception that the sign of vorticity is reversed. Figure 2(a) shows a mesoanticyclone whereas Figure 3(a) shows a mesocyclone. Hereafter, the term "mesocyclone" is implicitly used for both mesocyclones and mesoanticyclones.

Mesocyclones are typically observed at mid levels (5-10 km altitude), and they can be attributed to low-level convergence and to high-level divergence (e.g., Brown & Wood, 1991). In that sense, one can state that the main updraft is rotating, i.e. is associated with vertical vorticity. Therefore, a supercell storm is often defined as "a storm with a mesocyclone". This is probably the most unequivocal criterion for its detection (Moller et al., 1994). A supercell storm may become tornadic when the mesocyclone extends from mid levels to low levels. Such an extension is not seen in the storms investigated here.

2.3. Environment

We used weather maps, satellite images (Meteosat), the operational soundings from Payerne, data from an automatic mesonetwork and wind profile measurements from the Doppler

radar (see Section 2.1.) for characterizing the meteorological environment in which the storms develop. The mesonetwork of ground stations contains 72 stations. Meteorological variables (e.g., temperature, dew point temperature, precipitation and wind) are registered every 10 min. Radiosoundings are made twice per day (0000 and 1200 UTC) by the SMI in Payerne. The geographical location of the ground and sounding stations is depicted in Figure 1.

Important parameters characterizing the environment of convective storms are the convective available potential energy (CAPE, see Weisman & Klemp, 1982), the bulk Richardson number (BRN, see Weisman & Klemp, 1984) and storm-relative helicity (SRH, see Droegemeier et al., 1993). The equations and procedures to calculate these parameters are given in the Appendix. The CAPE is a measure of the instability of the atmosphere, and BRN combines CAPE and vertical shear (in the lowest 6 km) into a dimensionless number. The quantity SRH is related to the across-shear propagation of a storm (Rotunno, 1993) where the term “across-shear” refers to that component of the motion vector of the storm that is perpendicular to the shear vector of the environmental wind profile, typically calculated over the lowest 3 km above the ground. Based on numerous studies in the U.S., supercell storms are expected when “some” CAPE is available (CAPEs > 1500 J kg^{-1} are typical for “warm season” storms over the U.S. plains but supercell storms with smaller CAPEs may occur in other regions and climates), when BRN is on the order of 10-40, and when the absolute value of SRH is more than “somewhere around” 100-150 m^2 s^{-2} (Moller et al., 1994). To calculate these parameters, one needs “representative” profiles of temperature, dew point temperature, wind direction, wind speed, and (for SRH) a good estimate of storm motion. The profile data from the Payerne sounding was used for this purpose. Additional data are used to modify these profiles in such a way that they represent the inflow side of the storms as well as possible. Details about these modifications are given in Section 4 and in Table 2.

3. Wind damages and low-level radar data

The three investigated storms are called storms 1, 2 and 3 hereafter. The storm tracks, derived from the SMI-radar images, are depicted in Figure 4. In this section we document the hail and wind damage at the ground and the associated radar patterns at low levels. Figure 5 gives an overview on the hailswaths (derived from damage data of the Swiss hail insurance company, for details see e.g., Willemse & Schiesser, 1996) and the locations of the most severe wind gusts (derived from newspaper reports). By considering the radar patterns, one has the possibility of retrieving the time of the damaging wind gusts with a precision of a few minutes. In Section 4, we will then discuss the meteorological environment and the radar evolution of the storms as observed in the hours preceding the damage on the ground.

The wind damage in each storm was probably caused by straight-line winds rather than by tornadoes. No eyewitness reports of tornadoes are known to the authors although some newspaper articles speculated on the occurrence of tornadoes. The radar observations yield additional evidence for the lack of occurrence of tornadoes: the identified meso(anti)cyclones did not extend to low levels, and the low-level shear signatures associated with the damage tracks were significant but not extraordinary. We cannot exclude that tornadic whirls occurred along the gust front outflows, but we believe that such whirls, if present, were only responsible for a minor part of the damage.

Storm 1 on 21 July 1992 was part of a mesoscale convective system that caused severe damages in France, Germany, Austria, and Switzerland (Haase-Straub & Hauf, 1994). A summary on the evolution of the system in Switzerland is given by Huntrieser et al. (1994). In Switzerland north of the Alps, the largest number of communities (584 out of 2400) since 1971 was affected by hail damage. Damage due to heavy wind and floods occurred as well. Five persons were killed. Several storms were identified from the radar data. The storm considered here produced a hailswath of about 170 km in length and 25 km in width (see Figure 5(a)). Two tracks of severe wind damage were deduced from newspaper reports, one of them being located about 20 km south of the ETH-radar. Broken and thrown trees in forests and plantations blocked roads and railway lines on this track. Roofs were damaged or blown off. The damage track was more or less a straight line, about 25 km long.

Figure 6(a) shows radar reflectivity and Doppler velocity some 100 m above the ground at the time (1703 UTC) when the Doppler velocity reached its maximum near the starting point of the damage track. A bow-shaped convergence line, marked with a “cold front” signature, crossed the damage track. The subsequent radar scans (not shown here) reveal the evolution of

the gust front moving in a ENE-direction and allow the time to be fixed when the wind gusts reached the end point of the damage track (1720 UTC). The peak Doppler velocities decreased with time since the viewing angle of the radar became more and more perpendicular to the direction of the heaviest wind gusts (in the ENE-direction). A ground mesonet station near the end of the damage track (see Figure 5(a)) registered the peak wind speed (32 m s^{-1}) between 1720 and 1730 UTC. We can conclude that the heaviest wind gusts on the damage track occurred most probably between 1700 and 1720 UTC.

On 20 August 1992, storm 2 produced a hailswath about 70 km long and 12 km wide (Figure 5(b)). Severe wind damages were reported from five communities. Broken trees blocked roads, two aisles in the forests are documented, and buildings were severely damaged in one community. The damage track has a length of about 12 km. On the whole, the damage due to wind was less severe than in storms 1 and 3.

The low-level Doppler pattern shows substantial convergence and some azimuthal shear at the time (1643 UTC) when the strongest radar echo passed the starting point of the damage track (Figure 5(b)). The Doppler velocity indicates motion towards the radar on the damage track. This is consistent with the wind measurement from the mesonet station in Wynau (WY in Figure 5(b)), near the end of the damage track. There, the wind direction for the period of interest was mainly from S-SW. The Doppler signal of the wind gust is not detectable since the radar was in an unfavorable viewing angle. A convergence/shear line is nevertheless identifiable (“cold front” signature in Figure 6(b)), and we determine the time when the damaging wind gust occurred (between 1640 and 1700 UTC) from the passage of this shear line. This period is in a good agreement with one eyewitness observation (1645 UTC) from Langenthal (LA in Figure 5(b), lying in the middle of the damage track) and with the wind measurements in Wynau, indicating that the strongest wind speeds (up to 18 m s^{-1}) occurred between 1640 and 1700 UTC.

One day later, storm 3 was responsible for severe damage due to hail and wind in Central Switzerland. The hailswath was about 140 km long and 25 km wide (Figure 5(c)). Hail was lying in layers 50 cm thick at some locations after the passage of the storm. Wind damage was reported from many locations inside of the hailswath. The most severe damage occurred along a track of about 25 km in length (as in case of storm 1). The roof of a church was blown off and a plantation with 3500 fruit-trees was devastated. Parts of forests were destroyed, many trees were broken, and many buildings were badly damaged. Ten percent of the protective forest on the northern flank of Mount Rigi (location see Figure 5(c)) collapsed. Vast damage occurred in

the forests further east where trees were uprooted and blocked the roads. Less severe and more isolated wind damage were reported from locations up to about 15 km in the south of the track (e.g., in Luzern, LU in Figure 5(c)). In summary: the damage due to wind on this track was the most severe of the three storms.

The radar pattern at 1618 UTC shows two convergence/shear lines (“cold front” signatures in Figure 6(c)). The northern line is directly associated with the damage track. The time of occurrence of the damaging wind gust can be determined in the same manner as in the case of the other two storms. This yields the period 1615-1635 UTC which is again in a good agreement with the wind measurements of the closest mesonet station in Luzern (see Figure 5(c)). There, a peak wind gust of 32.5 m s^{-1} was registered between 1610 and 1620 UTC. The wind direction was from the west which means that, as in storm 2, the peak wind gusts remained undetected by the Doppler radar since the radar scanned the storm from NNE, nearly perpendicular to the direction of the wind gust.

One can summarize that low-level Doppler radar data are an excellent tool for retrieving the time of occurrence of severe wind damage on the ground. When doing this, one has to distinguish between two situations: if the radar beam is oriented more or less parallel to the direction of the wind gust, there is the possibility of identifying and tracking the wind maximum. If not, there is still the possibility of identifying convergence or shear lines and of attributing these lines to the strong wind events. The precision of the estimated time periods is of the order of some minutes. In the investigated cases, additional wind measurements on the ground enhance the confidence into the estimated time periods. It will be shown in the next section that a good estimate of the time when the damage occurred is important for obtaining more insight into the origin and development of the damaging wind gusts.

4. The storms

The main purpose of this section is to summarize the synoptic and meso-meteorological environment of the storms, and to document the evolution of the storms seen with radar.

4.1. Storm 1 (21 July 1992)

The synoptic and meso-meteorological setting of storm 1 has been discussed elsewhere (e.g., Heimann, 1994). Therefore, we will only summarize the most important aspects of the storm environment. At 0000 UTC, the eastward movement of a 500 hPa trough towards central Europe was increasing the southwesterly flow at mid-levels over Switzerland (Figure 7(a)). The surface map at 1200 UTC (Figure 7(b)) shows a depression over the North Sea, and the associated cold front was slightly retarded west of Switzerland. The release of convection was undoubtly favored by the proximity of the cold front, but the satellite pictures suggest that the orography played a crucial role in determining the locations of the developing thunderstorms. At 1400 UTC, convection has started along the Jura mountains (dashed arrows in Figure 8), leading to two supercell storms that caused a first damage track in northwestern Switzerland (region of Basel, location see Figure 1). The initiation of convection was slightly retarded in the pre-alpine regions south of Bern (location see Figure 1). It was in that region where storm 1 developed (solid arrow in Figure 8).

The Payerne sounding (1200 UTC, Figure 9(a)) revealed good conditions for development of severe thunderstorms. The airmass was humid and unstable (CAPE=1014 J kg^{-1}, see Table 2), and the wind speed increased continuously from the ground up to 3 km (see the hodograph in Figure 9(b)). The BRN was 29 (Table 2), indicating that supercell storms are possible. The SRH was 23 m^2 s^{-2}, being far below the critical limit for supercell storms. The spatial representativity of the radiosounding was judged with data from the ground mesonet and with VAD wind profile measurements obtained with the ETH radar. The ground measurements of temperature and humidity in Waedenswil (location see Figure 1), taken about 1 hour ahead of the evolving storm (1630 UTC), were nearly the same as the ground measurements of the operational sounding. Therefore, no modification of the Payerne sounding regarding temperature and humidity was made. The VAD wind profile (ETH radar, 1700 UTC) was used to add a modified wind hodograph in Figure 9(b). The hodograph shows a change of the wind at various altitudes, compared with the operational Payerne sounding. The changes in the wind profile are most probably caused by the combined effects of orography and the evolving storm systems.

As a result, BRN decreased a bit but SRH increased dramatically and reached 256 $m^2 s^{-2}$ (Table 2) which is in a good agreement with the supercellular character of the evolving storm.

Volume-scan radar measurements through the storm started at 1600 UTC, a time when the storm was already fully developed. The radar operations were briefly interrupted for technical reasons between 1640 and 1650 UTC. Figures 9(c) and 9(d) show the damage track and the time evolution of DV, H_{45} and the range in altitude of the identified MVSs. Figure 9(e) depicts schematically the locations of low-level convergence ("cold front" signature) for 1633, 1653 and 1708 UTC, of high-level divergence (dotted curves) and the MVSs (solid circles) at 1633 and 1708 UTC, and of the damage track (heavy solid line).

The first MVS (between 1603 and 1638 UTC) fulfilled the criteria of a mesocyclone to exist (vertical extent > 4 km and duration > 30 min). The second one was scanned during 20 min (1703-1723 UTC). After 1723, the MVS probably continued to exist but was not properly tracked because the storm passed the radar site at a close distance. We assume that the second MVS fulfilled the criteria of a mesocyclone as well.

The two mesocyclones were clearly separated. The initiation of the second mesocyclone was associated with the rapid growth of a new convective cell, shown in Figure 9(d) by the increasing values of the parameters H_{45} and DV between 1653 and 1723 UTC. This period of rapid cellular growth coincided with the period of the damage (see vertical arrow in Figures 9(c) and 9(d)). This agreement in time has to be kept in mind and will be discussed further in Section 5. Figure 9(e) yields additional insight into the interrelationship between the discussed Doppler signatures. First, one notes that the MVSs occurred at the southeastern edge of the zone of high-level divergence. Second, the signature of low-level convergence was located below the MVS and the signature of high-level divergence at 1708 UTC. The situation was a bit different 35 min earlier. At that time, the convergence line (hereafter called the "gust front") already started to propagate away from the MVS and the signature of high-level divergence. The northern edge of the gust front appeared to form the starting point of the damaging wind gust. This starting point could be identified at 1653 UTC (see Figure 9(e)), immediately after the deadstart of the radar measurements.

4.2. Storm 2 (20 August 1992)

The synoptic situation in the free atmosphere (500 hPa, see Figure 10(a)) was similar to that on 21 July 1992. The 500 hPa trough was associated with a low at sea level whose center was

situated over Belgium at 1200 UTC (see Figure 10(b)). A convergence line west of Switzerland was associated with cloud bands (see the satellite picture at 1400 UTC, Figure 11). Heavy thunderstorms were embedded in the northern parts of the cloud bands over southern Germany and eastern France. The developing storm is marked with a solid arrow in Figure 11. The storm originated at the eastern side of the leading cloud band in the pre-alpine region south of Bern. The outbreak of this storm is thought to be the result of the combined effects of orography and the convergence line.

The Payerne sounding from 1200 UTC (Figure 12(a)) shows a CAPE of 1116 J m^{-2} (Table 2). This CAPE is released by a dewpoint temperature of 16.4^{o}C at the ground. A mesonet station on the inflow side of the storm (“Wynau”, see Figure 1) yielded a dewpoint temperature of 19^{o}C at 1630 UTC. We replaced the ground values of temperature and dewpoint temperature of the Payerne sounding with the values measured in Wynau (1630 UTC) and we obtained a marked increase of CAPE (2536 J m^{-2}, see Table 2). This would mean an increase of BRN (originally 42, see Table 2) if the wind profile remained unchanged. The BRN and SRH would then predict non-supercell storms only. However, a mountain station in the west (inflow side) of the storm (Chasseral, 1600 m MSL, see Figure 1) showed an increase of westerly winds from 4 m s^{-1} (1200 UTC) to 13 m s^{-1} at 1630 UTC whereas the low-level winds remained weak from the northeast (station Wynau). This change in the wind at 1600 m can possibly be attributed to the passage of the convergence line shown in Figure 10(b). A modified wind hodograph based on these measurements was inserted in Figure 12(b). As a result, the BRN remained almost constant whereas the absolute value of SRH increased (see Table 2) and reached the range for which supercell storms are possible.

The radar evolution of the storm is shown in Figures 12(c) to 12(e). Three cells could be identified (cells A, B and C, in Figure 12(c)). Cell A was associated with a mesoanticyclone whose duration was 35 min. Cell B developed some kilometers north of decaying cell A. This cell was the strongest, and it was associated with a new mesoanticyclone (duration ~ 40 min). The parameters DV and H_{45} reached values that were the largest of all three storms. Cell C was similar in strength as cell A, but a mesoanticyclone was not observable. Some MVSs appeared at low altitudes (below 5 km) in this cell, but the criteria of a mesoanticyclone were not fulfilled.

The most evident difference between storms 1 and 2 is that the former was right-moving whereas latter was left-moving. Therefore, one has to consider that storm 2 was basically a

mirror image of storm 1. Considering this one can state that the two storms have many similarities. For instance:

(a) Two cells, both associated with a meso(anti)cyclone, follow each other.

(b) The second cell was the strongest in both storms (compare the time evolution of the parameters DV and H_{45}).

(c) In both storms, one finds a close association between the damage tracks, low-level convergence, mid-level rotation, and high-level divergence (compare Figures 9(e) and 12(e)).

(d) The meso(anti)cyclones occurred near one edge of the regions of high-level divergence in both storms.

But, most importantly: *in both storms, the period of heavy wind coincided in time with the growing stage of the second cell* (compare Figures 9(c,d) and 12(c,d)).

4.3. Storm 3 (21 August 1992)

The weather situation on that day was such that only isolated thunderstorms, predominantly in mountainous regions, were expected. Weak flow from NE dominated in Northern Switzerland at low layers whereas southwesterly flow was still present at 500 hPa (see Figure 13). No frontal line can be identified that could explain the release of severe convection in Northern Switzerland. The Payerne sounding at 1200 UTC (Figure 15(a)) indicated less instability than on the day before. The CAPE was 205 J m^{-2} (see Table 2) and an inversion at 620 hPa seemed to inhibit the release of deep convection. BRN was extremely low (Table 2), indicating that supercell storms were unlikely. For these reasons, the observed outbreak of a large and damaging thunderstorm was astonishing.

On the other hand, one can find explanations for the occurrence of heavy storms from the meso-meteorological and orographic setting. First, the shear at low layers (0-3 km above ground) was quite large (see Figure 15(b)). This fact led to a moderate SRH (130 m^2 s^{-2}), indicating that supercell storms can develop. Secondly, the observed inversion might have had a selective effect on convection: deep convection was suppressed by the inversion layer in most of the observational area. At some few places, however, convection may have penetrated the inversion layer. There, a large storm may have developed without competition from neighboring storms. Thirdly, one has to take into account local effects on the distribution of humidity, instability and wind and, hence, on the release of deep convection. Considering the measurements of two mesonet stations (Luzern, at 456 m MSL and Napf, at 1406 m MSL) ahead of the storm

leads to an increase of CAPE, BRN and SRH (see Table 2). The BRN is now in a range that predicts the occurrence of supercell storms.

The satellite picture in Figure 14 shows that the Jura mountains were an important source of convection on that day. Storm 3 developed in the Jura mountains north of Geneva (solid arrow in Figure 14). The path of the storm is given in Figure 4, and the evolution of the storm between 1500 and 1700 UTC is shown in Figures 15(c) to 15(e). At 1543 UTC, the storm was composed of several cells, each of them producing a distinct signature of high-level divergence (dashed ellipses in Figure 15(e)). Two MVSs were detectable at mid-levels. At 1613 UTC, two regions of high-level divergence can be identified. The two regions merged, and just one large signature of high-level divergence was seen at 1643 UTC. The two MVSs, clearly separated at 1543 UTC, merged in a similar manner. At 1613 UTC the merging of the MVSs was already completed. Note that the merging process led to an exceptionally large MVS, now having a diameter on the order of 10-15 km (see Figures 15(e) and 3(a)). This is about the double of the characteristic diameter (6 km) of the other observed MVSs (see Figures 2(a), 9(e) and 12(e)). The criteria of a mesocyclone were fulfilled, as shown by the time evolution of the MVS in Figure 15(d). For simplicity, only the northern MVS is depicted in this figure as long as the northern and southern MVSs were separated. The duration of the mesocyclone was about 70 min. This is the longest lifetime of a mesocyclone discussed in this paper.

The time evolution of DV and H_{45} is shown in Figures 15(c) and 15(d). The parameters represent peak values of the whole storm system. The time variation of these parameters is somewhat smaller than in case of storms 1 and 2. It is not possible to identify individual cells from these curves alone. The reason is that several cells of similar strength coexist at the same time. The damaging winds at the ground occurred, as in storms 1 and 2, about 40 min after the first appearance of the MVS. The damage track is associated with an increase of DV (compare Figures 15(c) and 15(d)). Thus, as in storms 1 and 2, the damage track appeared to coincide with an increase in updraft. In contrast to storms 1 and 2, the strengthening of the storm is not supported by the time evolution of H_{45}. The following explanation can be offered: the damage tracks of storms 1 and 2 could be attributed to the formation of new cells that were clearly separated from the former ones. In storm 3, however, existing cells merged and tended to form one large cell. This merging process appeared to modify the organization of convection (expressed e.g., in terms of the size of the mesocyclone), and this change might have modified the relationship between the parameters H_{45} and DV.

5. Discussion

5.1. Comparison with the U.S. supercell spectrum

The first important result of this study is that the investigated storms were supercellular and produced non-tornadic wind damage. To understand this finding, it is interesting to place the three storms into the U.S. storm spectrum. U.S. studies divide supercell storms into “low precipitation” (LP), “classic” and “high-precipitation” (HP) storms (e.g., Moller et al., 1994). Tornadoes are mainly expected in classic supercell storms whereas HP storms tend to produce torrential rainfall, severe hail, and severe downbursts. HP-storms are characterized by substantial precipitation in the mesocyclone. Brooks & Doswell (1993) discussed the potential formation of extreme winds in HP storms. Their conceptual model implies that weak storm-relative winds at mid-levels are a necessary condition for the formation of extreme non-tornadic winds at the ground. As a result, a large amount of rain would be wrapped around the rotating updraft. Evaporation and the associated cooling would be so large that a strong downdraft is produced. This downdraft might cut off the initial storm and initiate a new cell with a mesocyclone at a neighboring place. In that sense, one can classify HP storms as multicell storms as well. The main difference to multicell storms composed of “ordinary” cells is that the individual cells of HP storms are associated with rotating updrafts, propagate in a specific manner and remain for more than 30 min in a mature stage. Ordinary cells with non-rotating updrafts typically remain for 15-30 min in a mature stage (e.g., Browning, 1977).

The conceptual model of Brooks & Doswell (1993) corresponds with the evolution of storms 1 and 2. The mean storm-relative winds at a layer of, say, 3-7 km are on the order of less than 10 m s^{-1} (see Figures 9(b) and 12(b)). The storms show a sequence of two cells that were associated with meso(anti)cyclones. The second cell was triggered by the gust front outflow of the first cell, and the damage tracks were associated with the same gust front outflow. The radar data confirmed that the meso(anti)cyclones were filled with precipitation. The RHI section from Figure 2(b), for instance, taken through the core of a mesoanticyclone, shows reflectivities of 20-50 dBZ reaching the ground. The two storms were most probably HP-storms.

The situation is more complex in storm 3. The mean storm-relative winds at 3-7 km were a bit larger (on the order of 10 m s^{-1}, see Figure 15(b)) than in case of the other two storms. As a consequence, the downdraft might have been formed more slowly, and the gust front outflow might have been more in phase with the storm motion. Such a behaviour explains partly the more continuous propagation of storm 3, compared to storms 1 and 2. Thus, the conceptual

model of Brooks & Doswell (1993) is not unrestrictedly applicable to storm 3. However, the storm was a HP-storm since the mesocyclone was filled with precipitation (see the RHI-section through the mesocyclone shown in Figure 3(b)).

The model of Brooks & Doswell (1993) cannot explain the agreement in time between the damage tracks and the strengthening updrafts. It is possible that this agreement occurs by pure chance in the three storms. It is, however, also possible that the gust front outflows are accelerated by effects that are related to the developing updrafts (e.g., increase of convergence or vorticity at low altitudes). These open questions need to be clarified with a more detailed analysis of the data, with additional radar measurements (e.g., Dual-Doppler measurements), and possibly with numerical model simulations.

5.2. Implications for nowcasting

The existing literature on supercell storms indicates that the presence of a mesocyclone is a good indicator for an increased likelihood of severe convective weather (hail, floods, severe winds, tornadoes). The present study confirms this statement for hail and severe non-tornadic winds. The most important finding of this study from the point of nowcasting is that developing supercell storms are precursors of severe wind damage at the ground. A lead time of 40-55 min between the first detection of meso(anti)cyclones and the first occurrence of heavy wind damages at the ground has been found in three supercell storms. This result corresponds to U.S. studies on the relationship between mesocyclones and tornadoes. Burgess (1976), for instance, found a mean lead time of 36 min from mesocyclone detection to tornado touchdown. Two important differences to that study, however, should be mentioned. Firstly, the damage tracks discussed in this paper are most probably caused by non-tornadic winds. Secondly, the damage tracks were not associated with an extension of the mid-level mesocyclone to low levels.

Hereafter, we summarize important aspects in the nowcasting of supercell storms. This task can be splitted as follows.

(a) *Forecasting the initiation of supercell storms from a given meso-meteorological setting*. Three points are important:

- Role of orography in the initiation of severe thunderstorms. Synoptic factors, such as fronts or convergence lines, might contribute to an overall destabilisation of the atmosphere. But, at the end, it’s orography and solar radiation which steer the initiation of deep convection at

preferred (but not always the same) locations. Satellite data are a useful tool for identifying orographically induced convection at an early state. This aspect is not new (e.g., Collier & Lilley, 1994; Messmer et al., 1995) but is nicely confirmed by the three analysed storm cases.

- Conditions in the inflow region of developing thunderstorms. Factors like stability and wind shear steer the motion and internal structure of the storms. To obtain an idea of whether the outbreak of supercell storms is possible one needs to know these conditions. The problem is that combined effects of orography and already developed storms lead to unpredictable modulations of the relevant parameters (temperature, moisture, wind field), thus hampering the spatial and temporal representativity of operational radiosoundings (e.g., Brooks et al., 1994). Continuous measurements from ground stations, wind profilers (e.g., Steiner & Richner, 1989) or weather radars are thought to be a great help in assessing such modulations on a more local scale.
- Weak storm-relative winds at mid-levels. The formation of HP storms with damaging wind gusts tends to be favored when the storm-relative winds at mid-levels are weak. Therefore, the forecaster needs an estimate of the most probable storm motion. Such an estimate can be obtained, for instance, from the radar patterns after the initial development of convective storms. Combining the motion vector with wind profile measurements allows an estimate of the mean storm-relative winds at mid-levels. Open questions are the boundaries in altitude over which the winds are averaged, and the upper limit for the wind speed that defines the "weak" storm-relative winds.

(b) *Detection of developing supercell storms*.

The most promising tool for detection and identification of supercell storms is a Doppler weather radar, being able to yield volume-scan data with a temporal resolution of 5 min. Doppler signatures of meso(anti)cyclones are possibly the most unequivocal identifiers of supercell storms (Moller et al., 1994). Signatures of high-level divergence and, possibly, low-level convergence support identification of such storms as well. The quantity H_{45} and specific reflectivity patterns (weak echo regions, hook echoes) yield potentially useful criteria when a non-Doppler radar only is available. At the present stage of our knowledge, no statement is possible about which combination of these quantities and criteria does the best job. A large sample of storms is necessary to obtain statistically well-founded prediction criteria.

After the detection of such a storm, one has the task of identifying the probable location of the damaging wind gusts. Two possibilities for treating this problem exist. One possibility is to

extrapolate the observed storm motion into the future, and to consider the lead time between MVS detection and the damaging wind gusts (typically 40-55 min). A second possibility is to identify and track the gust front outflow of dangerous storms with the help of low-level Doppler radar data. No statement on the skill of these methods can presently be made.

6. Conclusions

The main purpose of the study was to find criteria that contribute to improve the nowcasting of severe wind gusts associated with supercell storms. The time periods of the damage tracks were determined with the help of low-level Doppler data. A series of criteria has been investigated that document the development and evolution of the storms until the wind damage occurred. The following main results were found:

(a) The storms developed in hilly regions and propagated towards the plains of the Swiss midland.

(b) Meso(anti)cyclones were detected with the Doppler radar about 40-55 min before the heavy wind damages at the ground occurred.

(c) The storms were most probably “high-precipitation” supercell storms in the sense of Moller et al. (1994).

(d) The time periods of the damage tracks coincided with explosive cellular growth.

It is hypothesized that strenghtening updrafts play a role in the acceleration of already existing gust front outflows. Further analyses of severe wind-producing storms and numerical model simulations are required, in order to judge the importance of this hypothesis. A larger storm sample would allow statistical tests to determine the usefulness of the various criteria for identification of severe wind-producing supercell storms.

Acknowledgements. This work was partially performed within a National Research Program (NRP31) and was financially supported by the Swiss National Science Foundation under Grant 4031-033526. Hermann Gysi, Matthias Hänni, Donat Högl, Sascha Hümbeli, and Li Li contributed to the radar operations, to the hardware and software support and to the analysis of the data. The Swiss Meteorological Institute (SMI) provided the data from the operational radiosondes and the ground and radar networks. Two reviewers helped in the improvement of the manuscript. All these contributions are gratefully acknowledged.

APPENDIX

Mathematical definitions of BRN, CAPE, and SRH:

BRN — Bulk Richardson Number (after Weisman and Klemp 1984)

$$BRN = \frac{CAPE}{\frac{1}{2}(\bar{u}^2 + \bar{v}^2)}$$

where $\bar{u}$ and $\bar{v}$ represent the E and N components of the vector difference between the density-weighted mean wind over a 6-km depth and a representative surface layer (lowest 500 m) wind.

CAPE — Convective available potential energy (J m^{-2})
(after Weisman and Klemp 1982)

$$CAPE = g \int_{LCL}^{TOP} \frac{\Theta(z) - \bar{\Theta}(z)}{\bar{\Theta}(z)} dz$$

where g = 9.81 m s^{-2} (mass acceleration of the earth)
Θ = Potential temperature (K) of an air parcel starting at LCL and raising moist adiabatically to cloud top (TOP)
$\bar{\Theta}$ = Potential temperature (K) of the environment
z = height (m)
LCL = Lifting condensation level, defined by lifting average temperature and moisture (expressed as water vapor mixing ratio) in the lowest 50 mb layer to the condensation level (after Fankhauser and Wade, 1982, p. 24)

SRH — Storm-relative helicity (m^2 s^{-2}), integrated over a layer of 3 km above the ground (after Moller et al. 1994).

$$SRH = -\int_0^z k \cdot (V - C) \times \frac{\partial V}{\partial z'} dz'$$

k = unit vector in the vertical

z’ = height (above ground)

V = horizontal wind vector

C = storm motion vector

z = assumed inflow-layer depth, here set to 3 km above the ground

SRH is minus twice the signed area swept out by the storm-relative wind vector between 0 and h on a hodograph diagram (e.g., Figures 9(b), 12(b) and 15(b)). The parameter is a measure of streamwise vorticity in the storm-relative inflow. This vorticity is tilted into the vertical when entering into the main updraft of a supercell storm, thus being the main source of rotating updrafts. Storm-relative helicity has become popular in the U.S. as a tool for prediction of supercell storms.

List of abbreviations and symbols:

BRN	Bulk Richardson number
CAPE	Convective available potential energy
D	Distance between the extremes in Doppler velocity of a VS
Δh	Vertical extent of a vortex signature
DV	Difference between the extremes in Doppler velocity of a signature of high-level divergence (positive values) or low-level convergence (negative values)
ΔV	Difference between the extremes in Doppler velocity of a VS
ΔV/2	Rotational velocity of a VS
ΔV/D	Shear between the extremes in Doppler velocity
ETH	Swiss Federal Institute of Technology
h	Mean altitude of a vortex signature
HP	“High-precipitation”
H_{45}	Height of the 45 dBZ contour
LCL	Lifting condensation level
LP	“Low-precipitation”
MSL	Mean sea level

MVS	Mesocyclonic (or mesoanticyclonic) VS
PPI	Plan position indicator
PRF	Pulse repetition frequency
RHI	Range-height indicator
SMI	Swiss Meteorological Institute
SRH	Storm-relative helicity
u, v	East and north components of the wind vector (m s^{-1})
UTC	Universal time coordinated (Greenwich time)
VAD	Velocity-azimuth display
VS	Vortex signature

REFERENCES

Alberoni, P.P., Nanni, S., Crespi, M. & Monai, M. (1996). The supercell thunderstorm on 8 June 1990: mesoscale analysis and radar observations. *Meteorol. and Atmos. Phys.*, **58:** 123-138.

Brooks, H.E. & Doswell III, C.A. (1993). Extreme winds in high-precipitation supercells. Preprints, 17th Conf. Severe Local Storms, Am. Meteorol. Soc., 173-177.

Brooks, H.E., Doswell III, C.A & Cooper, J. (1994). On the environments of tornadic and non-tornadic mesocyclones. *Wea. Forecasting*, **9:** 606-618.

Brown, R.A. & Wood, V.T. (1991). On the interpretation of single-Doppler velocity patterns within severe thunderstorms. *Wea. Forecasting*, **6:** 32-48.

Browning, K.A. & Ludlam, F.H. (1962). Airflow in convective storms. *Q. J. R. Meteorol. Soc.*, **88:** 117-135.

Browning, K. A. (1964). Airflow and precipitation trajectories within severe local storms which travel to the right of the winds. *J. Atmos. Sci.*, **21:** 634 - 639.

Browning, K. A. (1977). The structure and mechanisms of hailstorms. *Meteorol. Monogr.*, **16:** Am. Meteorol. Soc., 1-43.

Burgess, D.W. (1976). Single Doppler radar vortex recognition. Part I: Mesocyclone signatures. Preprints, 17th Conf. Radar Meteorol., Am. Meteorol. Soc., 97-103.

Burgess, D.W. & Lemon, L.R. (1990). Severe thunderstorm detection by radar. *Radar in Meteorology*, Atlas, D., Ed., Am. Meteorol. Soc., 619-647.

Changnon, S.A., Jr. (1970). Hailstreaks. *J. Atmos. Sci.*, **27:** 109-125.

Church, C., Burgess, D., Doswell III, C.A. & Davies-Jones, R. (1993). The tornado: its structure, dynamics, prediction, and hazards. *Geophys. Monogr.*, **79:** Am. Geophys. Union, 637 pp.

Collier, C.G. & Lilley, R.B.E. (1994). Forecasting thunderstorm initiation in north-west Europe using thermodynamic indices, satellite and radar data. *Meteorol. Appl.*, **1:** 75-84.

Dessens, J. & Snow, J.T. (1993). Comparative description of tornadoes in France and the United States. *Geophys. Monogr.*, **79:** Am. Geophys. Union, 427-434.

Donaldson, R. J. (1970). Vortex signature recognition by a Doppler radar. *J. Appl. Meteorol.*, **9:** 661 - 670.

Droegemeier, K.K., Lazarus, S.M. & Davies-Jones, R. (1993). The influence of helicity on numerically simulated convective storms. *Mon. Wea. Rev.*, **121:** 2005-2029.

Fankhauser, J.C. & Wade, C. (1982). The environment of the storms. *Hailstorms of the Central High Plains. Vol. 1: The National Hail Research Experiment.* Eds. C.A. Knight and P. Squires, Colorado Associated University Press, Boulder, Colorado, 5-34.

Geotis, S.G. (1963). Some radar measurements of hailstorms. *J. Appl. Meteorol.*, **2:** 270-275.

Haase-Straub, S.P. & Hauf, T. (1994). Significance of the events of 21 July 1992. *The squall line of 21 July 1992 in Switzerland and southern Germany - a documentation*. Haase-Straub, S.P., D. Heimann, T. Hauf and R.K. Smith, Eds., Research Report 94 - 18, DLR Oberpfaffenhofen, Germany, 7-12.

Heimann, D. (1994). Synoptic-data analysis. *The squall line of 21 July 1992 in Switzerland and southern Germany - a documentation*. Haase-Straub, S.P., Heimann, D., Hauf, T. and Smith, R.K., Eds., Research Report 94 - 18, DLR Oberpfaffenhofen, Germany, 13-26.

Houze, R. A. Jr., Schmid, W., Fovell, R. G. & Schiesser, H. H. (1993). Hailstorms in Switzerland: left movers, right movers, and false hooks. *Mon. Wea. Rev.*, **121:** 3345 - 3370.

Huntrieser, H., Schiesser, H. H., Schmid, W. & Willemse, S. (1994). The evolution of the 'mesoscale convective system' over Switzerland. *The squall line of 21 July 1992 in Switzerland and southern Germany - a documentation*. Haase-Straub, S.P., Heimann, D., Hauf, T. and Smith, R.K., Eds., Research Report 94 - 18, DLR Oberpfaffenhofen, Germany, 39-66.

Joss, J. & Lee, R. (1995). The application of radar-gauge comparisons to operational precipitation profile corrections. *J. Appl. Meteorol.*, **34:** 2612-2630.

Joss, J. & Waldvogel, A. (1990). Precipitation measurement and hydrology. *Radar in Meteorology,* Atlas, D., Ed., Amer. Meteor. Soc., 577-606.

Keeler, R.J. & Passarelli, R.E. (1990). Signal processing for atmospheric radars. *Radar in Meteorology,* Atlas, D., Ed., Am. Meteorol. Soc., 199-229.

Lemon, L.R. & Doswell III, C.A. (1979). Severe thunderstorm evolution and mesocyclone structure as related to tornadogenesis. *Mon. Wea. Rev.*, **107:** 1184-1197.

Li, L., Schmid, W. & Joss, J. (1995). Nowcasting of motion and growth of precipitation over a complex orography. *J. Appl. Meteorol.*, **34:** 1286-1300.

Messmer, B., Kolendowicz, L. & Schmid, W. (1995). Erkennung und Vorhersage von Hagel mit Meteosat-Daten. *Meteorol. Zeitschrift*, **4:** 187-195.

Moller, A. R., Doswell III, C. A., Foster, M.P. & Woodall, G. R. (1994). The operational recognition of supercell thunderstorm environments and storm structures. *Wea. Forecasting*, **9:** 327 - 347.

Rotunno, R. (1993). Supercell thunderstorm modelling and theory. *Geophys. Monogr.*, **79:** 57 -

73.

Schmid, W., Hümbeli, S., Messmer, B. & Linder, W. (1996). On the formation of supercell storms. Preprints, 18th Conf. Severe Local Storms, Am. Meteorol. Soc., 451-454.

Siggia, A. (1991). One pass velocity unfolding for VVP analysis. Preprints, 25th Conf. Radar Meteorol., Am. Meteorol. Soc., 882 - 888.

Steiner, A. & Richner, H. (1989). Deriving quality controlled wind profiles from Profiler moment data. *Meteorol. Rdsch.*, **42:** 101-108.

Waldteufel, P. & Corbin, H. (1979). On the analysis of single-Doppler radar data. *J. Appl. Meteorol.*, **18:** 532-542.

Waldvogel, A., Federer, B., Schmid, W. & Mezeix, J.F. (1978). The kinetic energy of hailfalls. Part II: Radar and hailpads. *J. Appl. Meteorol.*, **17:** 1680-1693.

Waldvogel, A., Federer, B. & Grimm, P. (1979). Criteria for the detection of hail cells. *J. Appl. Meteorol.*, **18:** 1521 - 1525.

Weisman, M.L. & Klemp, J.B. (1982). The dependence of numerically simulated convective storms on vertical shear and buoyancy. *Mon. Wea. Rev.*, **110:** 504 - 520.

Weisman, M.L. & Klemp, J.B. (1984). The structure and classification of numerically simulated convective storms in directionally varying wind shears. *Mon. Wea. Rev.*, **112:** 2479 - 2498.

Willemse, S. & Schiesser, H.H. (1996). A 45-year hailstorm climatology in Switzerland north of the Alps. Preprints, 18th Conf. Severe Local Storms, Am. Meteorol. Soc., 101-105.

Witt, A. & Nelson, S.P. (1991). The use of single-Doppler radar for estimating maximum hailstone size. *J. Appl. Meteorol.*, **30:** 425 - 431.

Figure captions

Figure 1. Location of all measuring devices, and of some cities, mountains and lakes referred to in this study. Schematic isolines of 1000 m altitude mark the boundaries of mountainous regions in the west of Switzerland ("Jura") and in the southeastern part of Switzerland ("Alps"). A more detailed representation of the orography is given in Figure 4.

Figure 2. (a) PPI and (b) RHI sections through the storm of 20 August 1992. The white bars mark the extremes of Doppler velocity of a MVS in (a), and a signature of high-level divergence in (b). The black bar in (b) marks a signature of low-level convergence.

Figure 3. As Figure 2 but of the storm from 21 August 1992.

Figure 4. The paths of storms 1 (21 July 1992), 2 (20 August 1992) and 3 (21 August 1992), based on the data from the two SMI-radars (see Figure 1). The time (UTC) of the first appearance of the 47 dBZ contour is given, and the storm centers (mass centroids of the 47 dBZ contour) are marked for each full hour. The orography is given in a grey scale.

Figure 5. The hailswaths (solid boundaries) and the tracks of severe wind damage (solid bars), for (a) storm 1, (b) storm 2 and (c) storm 3. The dashed line marks the boundary of Switzerland and the Bodensee. The squares mark mesonet stations referred to in Section 3. Additional locations referred to in the text are also indicated.

Figure 6. Damage tracks (solid arrows) and low-level radar patterns, for (a) storm 1, (b) storm 2 and (c) storm 3. The "cold front" signatures mark convergence lines or shear lines associated with the gust front outflows.

Figure 7. Weather maps at (a) 500 hPa 0000 UTC and (b) surface level 1200 UTC, for 21 July 1992. The surface map covers central Europe only. The radar range of the ETH-radar (120 km) is indicated with a circle in (b). Adapted from "Berliner Wetterkarte".

Figure 8. Meteosat picture (VIS) for 21 July 1992 1400 UTC. The ellipses mark the Lake of Geneva (left) and the Bodensee (right). The dashed arrows mark the Jura mountains. The solid arrow marks the developing storm 1.

Figure 9. (a) Skew T-log(P) diagram; (b) two wind hodographs (the arrow represents mean storm motion, the small dots and circles represent altitude in km MSL, and the shaded areas represent SRH); (c) DV-time diagram; (d) height-time diagram with H_{45} (squares), MVS altitudes (shaded areas), time of wind damage (solid bar) and a vertical arrow indicating the agreement in time between the damage and a growing cell; and (e) schematic presentations of low-level convergence ("cold front" signatures), MVSs (circles), high-level divergence (dashed

curves), and the damage track (solid bar) at specific times, for storm 1. The numbers in (e) indicate the altitude (km MSL) of the features.

Figure 10. Same as Figure 7 but for storm 2.

Figure 11. Same as Figure 8 but for storm 2 and without the dashed arrows.

Figure 12. Same as Figure 9 but for storm 2.

Figure 13. Same as Figure 7 but for storm 3.

Figure 14. Same as Figure 8 but for storm 3 and without the dashed arrows.

Figure 15: Same as Figure 9 but for storm 3.

Table captions

Table 1. The specifications of the ETH-Doppler weather radar and the measuring program for thunderstorm situations. For details on the Dual PRF mode see e.g., Keeler & Passarelli (1990).

Table 2. Mean storm motion and some environmental parameters, for three storms. CAPE, BRN and SRH were first calculated from the operational sounding in Payerne, 1200 UTC. Additional data (mesonet and radar) were then used to construct modified profiles and to recalculate CAPE, BRN and SRH.

-

Table 1.

TABLE 1.

Frequency	5.66 GHz
Wavelength	5.3 cm
Peak power output	250 kW
Pulse length	0.5 and 3 μs
Pulse repetition frequency (PRF)	250 to 1200 Hz
PRF for single PRF mode	1200 Hz
PRF for 3:2 Dual PRF mode[1]	1200/800 Hz
PRF for 4:3 Dual PRF mode[2]	1200/900 Hz
Unequivocal Doppler range for single PRF mode	$\pm$ 16 m s^{-1}
Unequivocal Doppler range for 3:2 Dual PRF mode[1]	$\pm$ 32 m s^{-1}
Unequivocal Doppler range for 4:3 Dual PRF mode[2]	$\pm$ 48 m s^{-1}
Antenna beam width	1.6° circular
Polarization	linear horizontal
Range	120 km
Scanning program	2 PPIs every 10 min
	RHIs every 5 min
	Sector volume scans every 5 min

[1]Used in this study. Folded Doppler data were corrected by eye.

[2]Preferable for operational applications

Table 2.

TABLE 2.

Storm No.	Date	Source	CAPE (J m^{-2})	BRN	Motion (Deg/m s^{-1})	SRH (m^2 s^{-2})
1	21 July 1992	Pay, 12 UTC	1014	29	217/14.4	23
		Pay+VAD ETH, 17 UTC[1]	1014	21	-	256
2	20 Aug 1992	Pay, 12 UTC	1116	42	207/9.1	-37
		Pay+WY/CH, 1630 UTC[2]	2536	41	-	-159
3	21 Aug 1992	Pay, 12 UTC	205	4	262/13.6	130
		Pay+LU/NA, 1530 UTC[3]	1178	28	-	166

[1]The wind measurements of the Payerne sounding were replaced by the VAD profile, measured with the ETH-radar at 17 UTC.

[2]The ground values of temperature and humidity of the Payerne sounding were replaced by measurements taken in Wynau at 1630 UTC. Wind measurements of Wynau and the Chasseral mountain (1599 m), obtained at 1630 UTC, were used to modify the wind profile of the Payerne sounding in the lowest 3 km.

[3]The ground values of temperature and humidity of the Payerne sounding were replaced by measurements taken in Luzern at 1530 UTC. Wind measurements of Luzern and the Napf mountain (1406 m), obtained at 1530 UTC, were used to modify the wind profile of the Payerne sounding in the lowest 3 km.

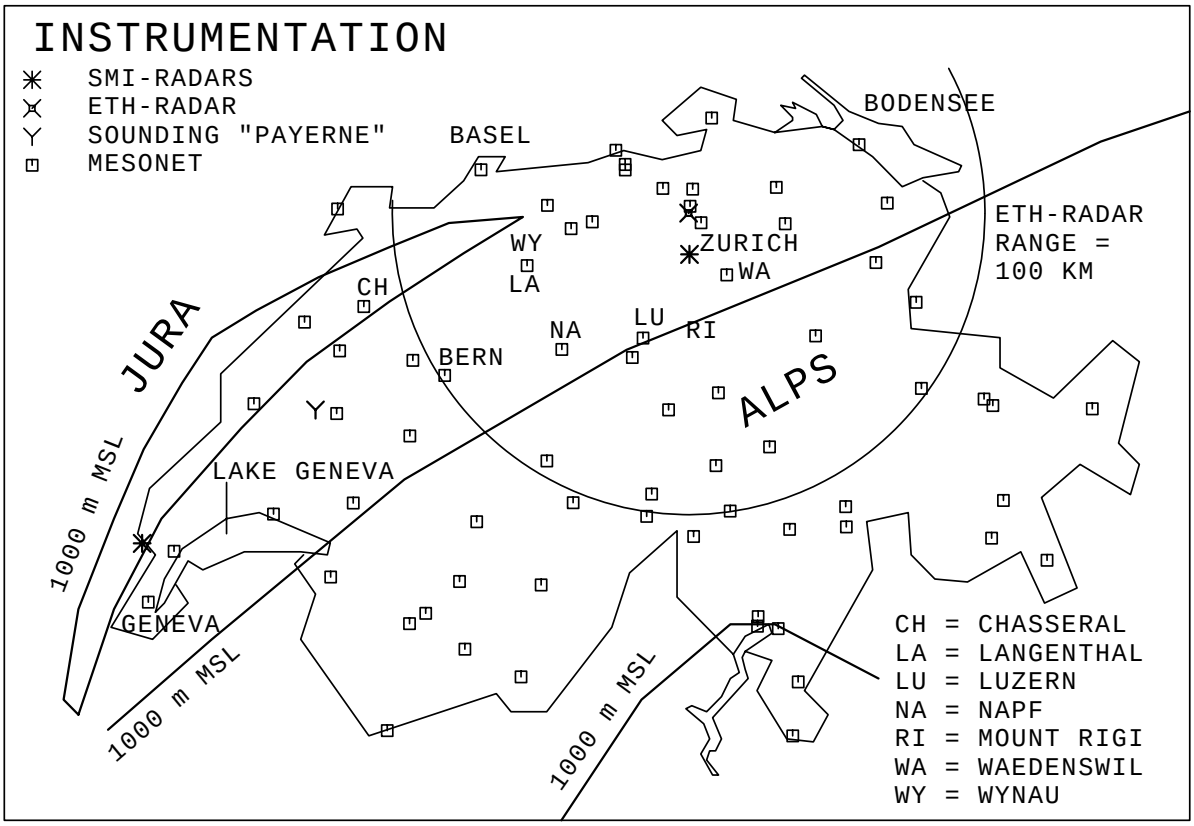
INSTRUMENTATION
SMI-RADARS
ETH-RADAR
SOUNDING "PAYERNE"
MESONET
BASEL
BODENSEE
ETH-RADAR
RANGE =
100 KM
ZURICH
WY
LA
WA
CH
NA
LU
RI
BERN
JURA
ALPS
Y
LAKE GENEVA
1000 m MSL
GENEVA
1000 m MSL
1000 m MSL
CH = CHASSERAL
LA = LANGENTHAL
LU = LUZERN
NA = NAPF
RI = MOUNT RIGI
WA = WAEDENSWIL
WY = WYNAU

Figure 1

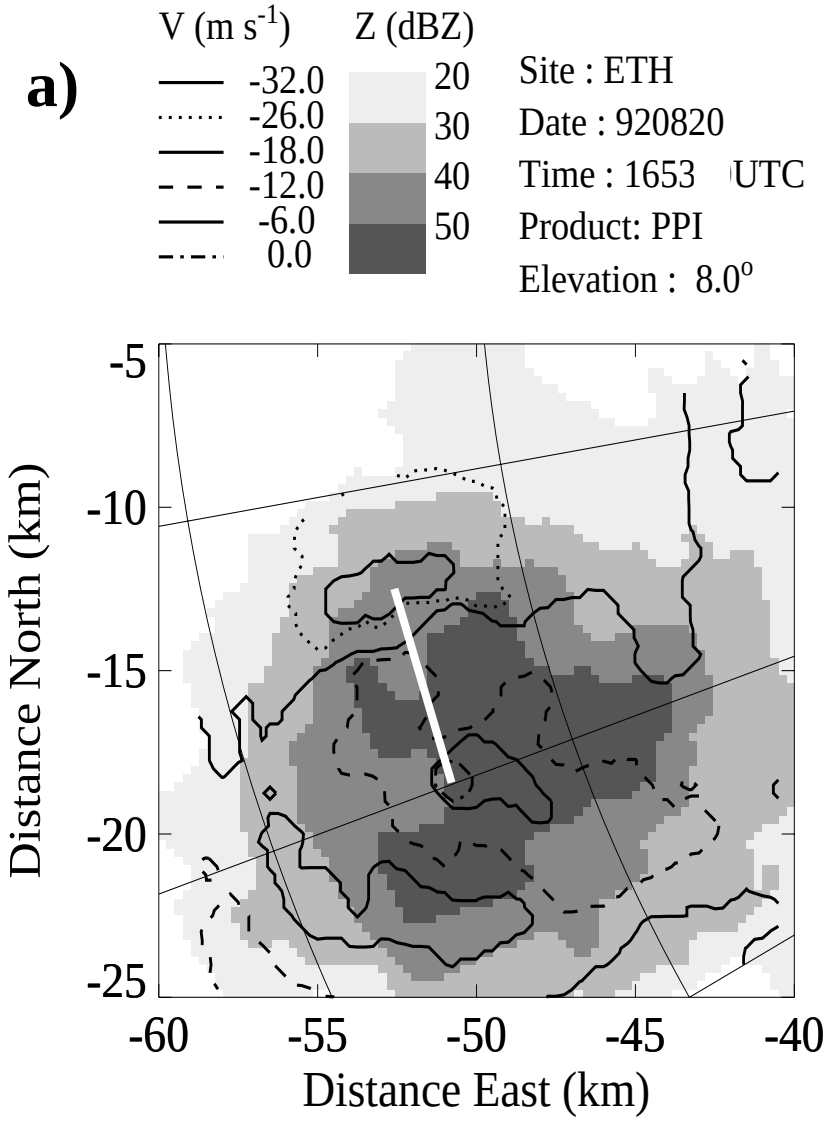
a)
V (m s-1)
Z (dBZ)
-32.0
-26.0
-18.0
-12.0
-6.0
0.0
20
30
40
50
Site : ETH
Date : 920820
Time : 1653 UTC
Product: PPI
Elevation : 8.0o
Distance North (km)
-5
-10
-15
-20
-25
-60
-55
-50
-45
-40
Distance East (km)

Figure 2(a)

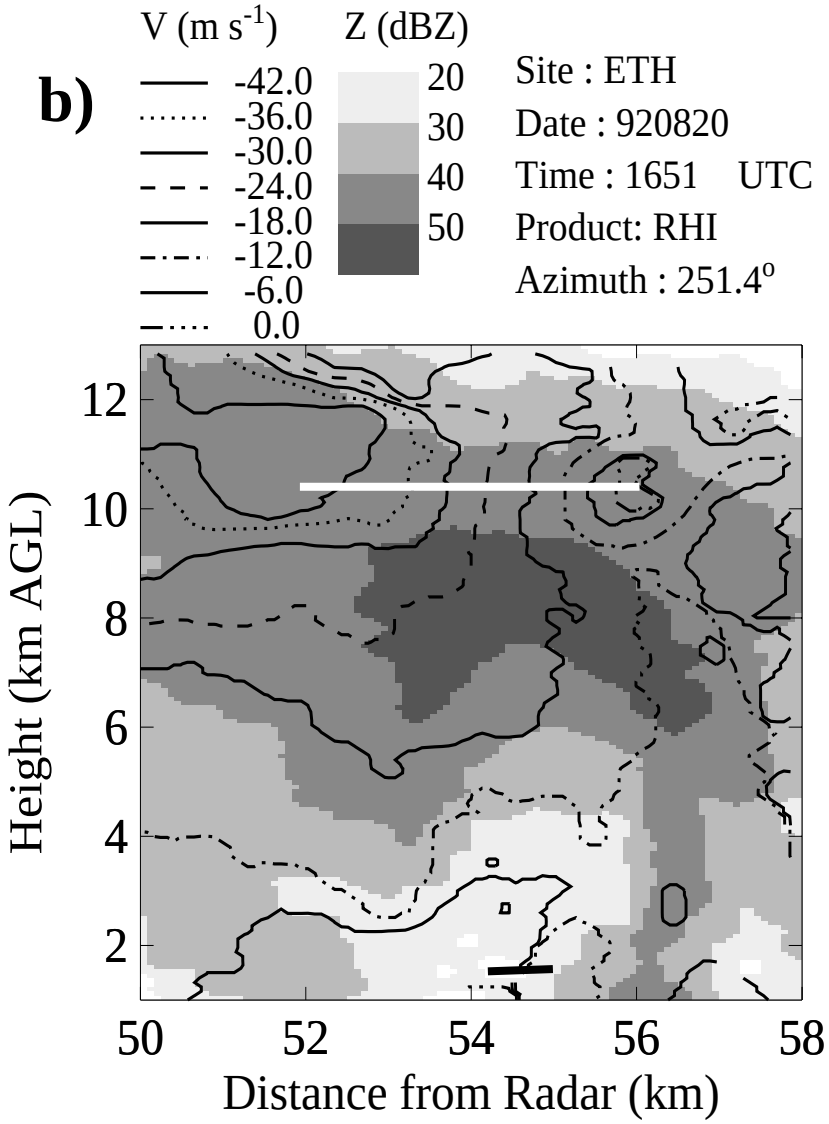
b)
V (m s-1)
-42.0
-36.0
-30.0
-24.0
-18.0
-12.0
-6.0
0.0
Z (dBZ)
20
30
40
50
Site : ETH
Date : 920820
Time : 1651 UTC
Product: RHI
Azimuth : 251.4o
Height (km AGL)
12
10
8
6
4
2
50
52
54
56
58
Distance from Radar (km)

Figure 2(b)

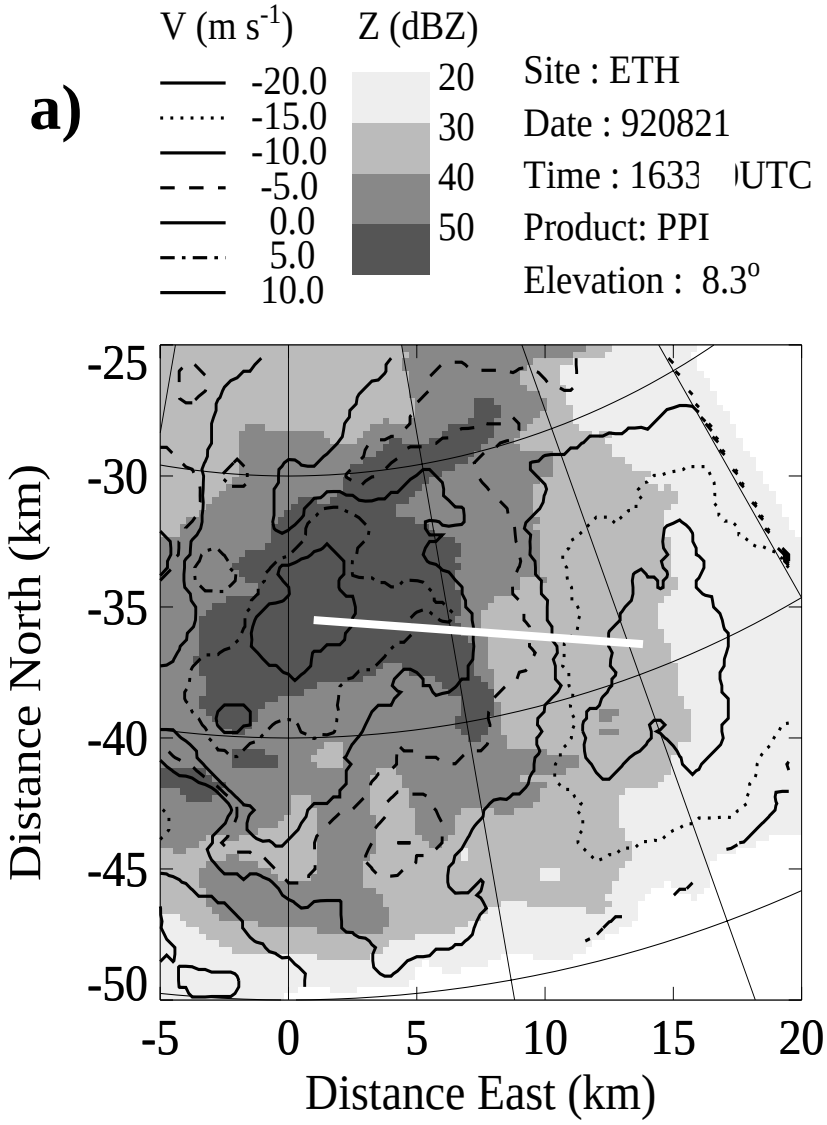
a)
V (m s-1)
Z (dBZ)
-20.0
-15.0
-10.0
-5.0
0.0
5.0
10.0
20
30
40
50
Site : ETH
Date : 920821
Time : 1633 UTC
Product: PPI
Elevation : 8.3o
Distance North (km)
-25
-30
-35
-40
-45
-50
-5
0
5
10
15
20
Distance East (km)

Figure 3(a)

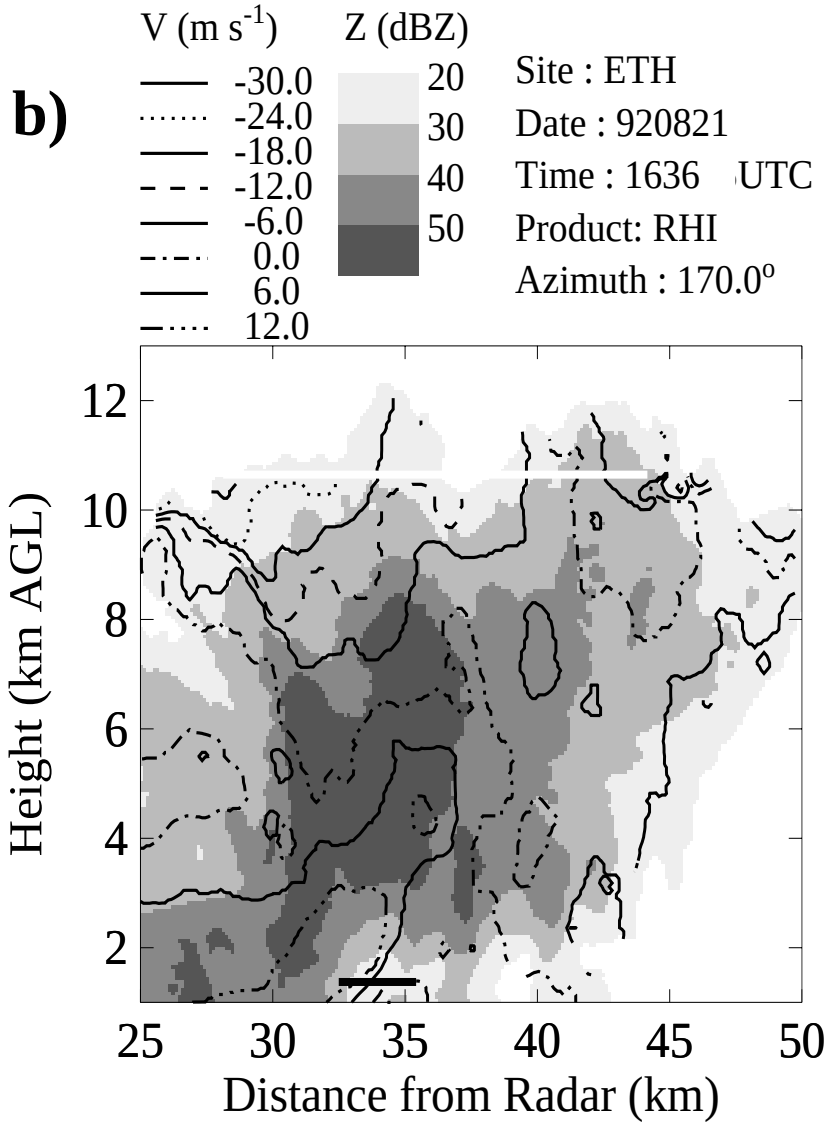
b)
V (m s-1)
-30.0
-24.0
-18.0
-12.0
-6.0
0.0
6.0
12.0
Z (dBZ)
20
30
40
50
Site : ETH
Date : 920821
Time : 1636 UTC
Product: RHI
Azimuth : 170.0o
Height (km AGL)
12
10
8
6
4
2
25
30
35
40
45
50
Distance from Radar (km)

Figure 3(b)

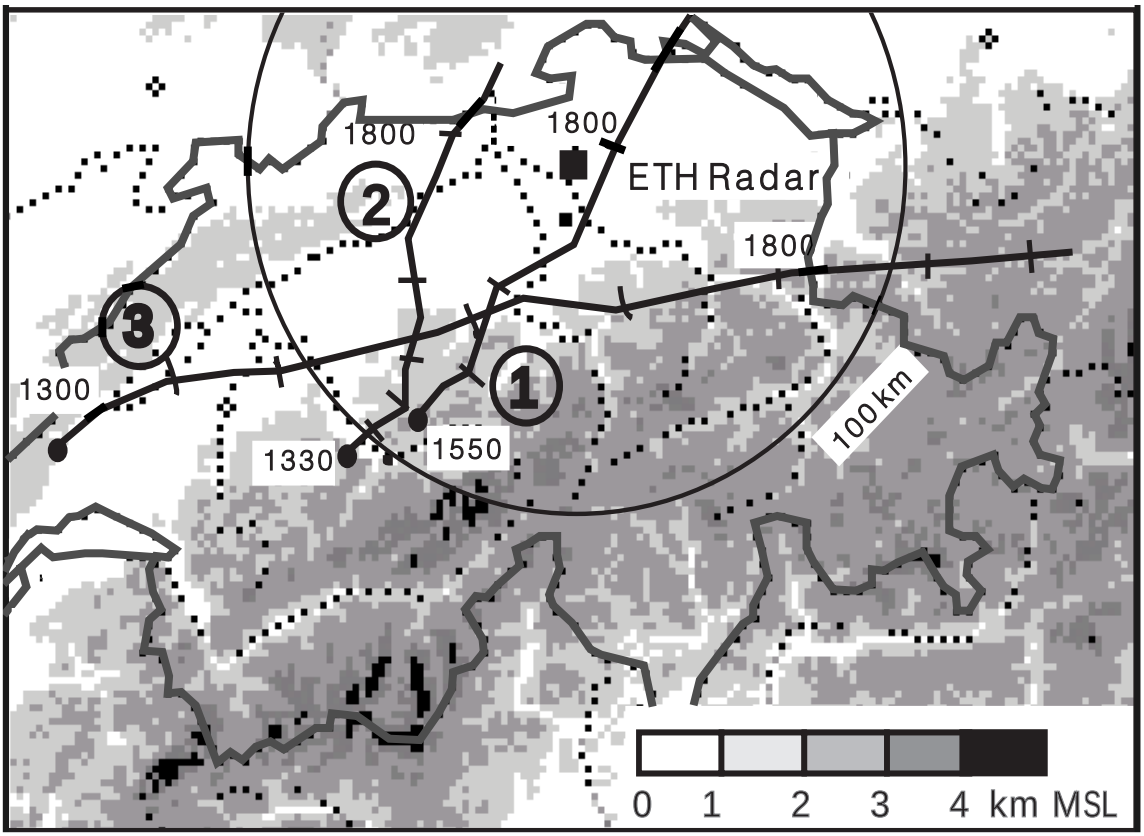
1800
1800
ETH Radar
1800
2
3
1
1300
1330
1550
100 km
0 1 2 3 4 km MSL

Figure 4

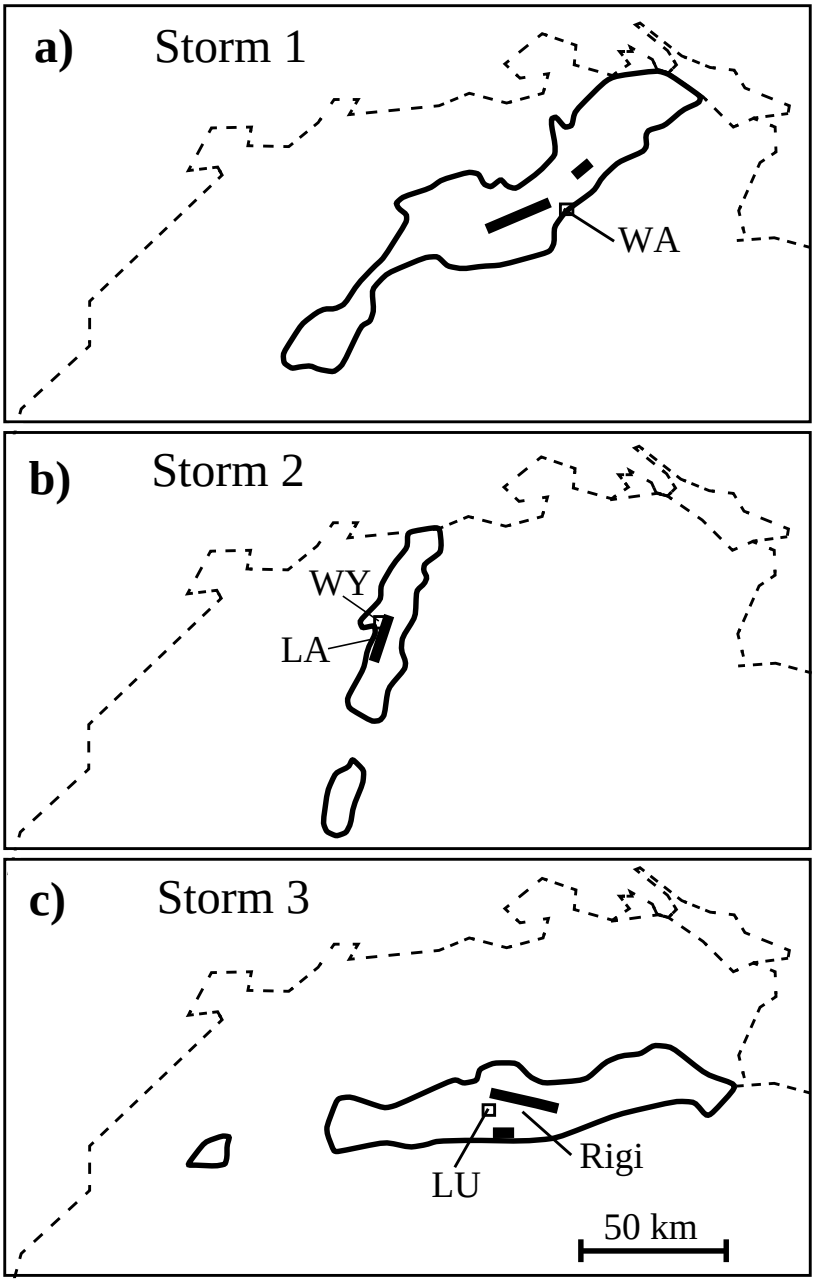

Figure 5

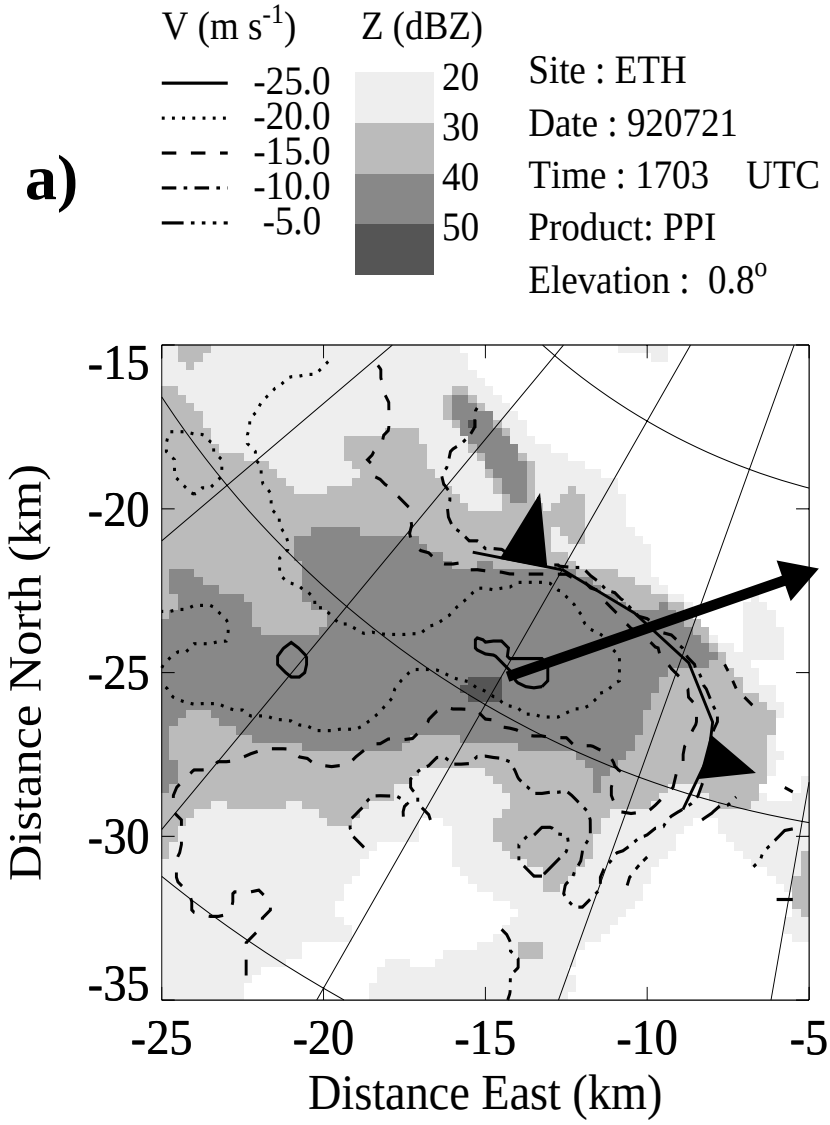
a)
V (m s-1)
-25.0
-20.0
-15.0
-10.0
-5.0
Z (dBZ)
20
30
40
50
Site : ETH
Date : 920721
Time : 1703 UTC
Product: PPI
Elevation : 0.8o
Distance North (km)
-15
-20
-25
-30
-35
-25
-20
-15
-10
-5
Distance East (km)

Figure 6(a)

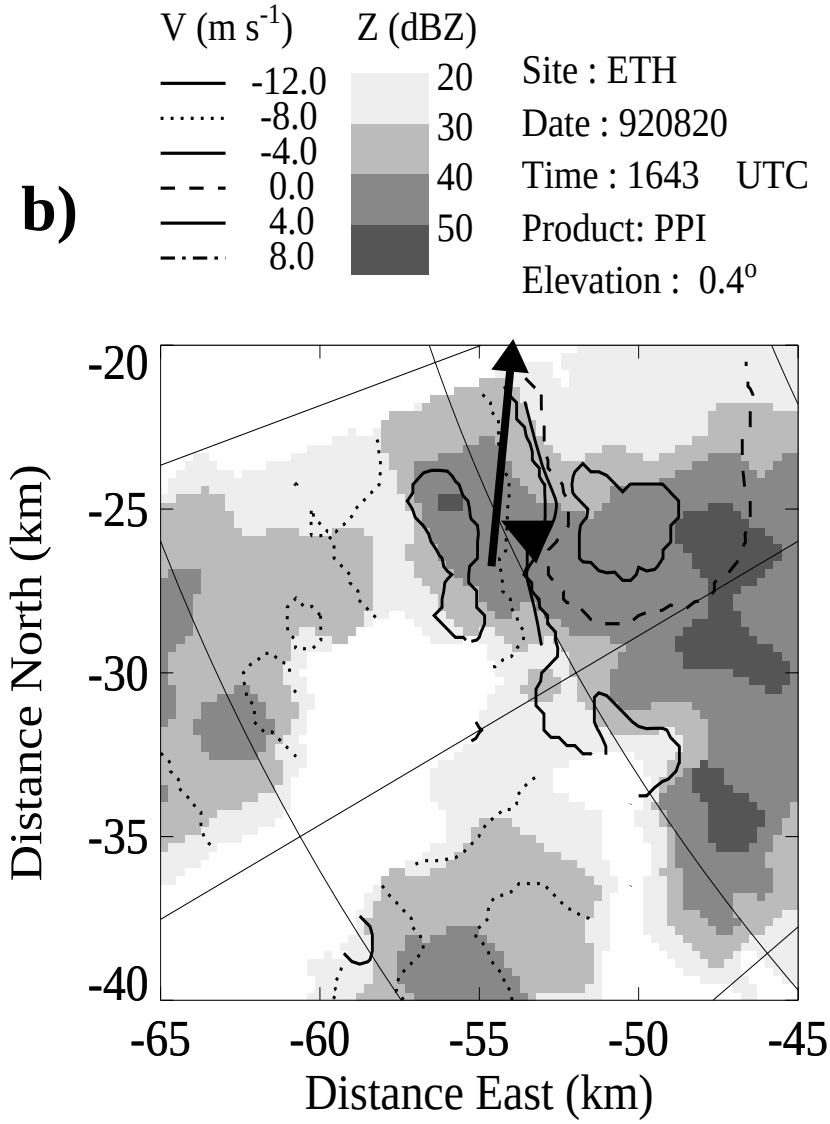
b)
V (m s-1)
Z (dBZ)
-12.0
-8.0
-4.0
0.0
4.0
8.0
20
30
40
50
Site : ETH
Date : 920820
Time : 1643 UTC
Product: PPI
Elevation : 0.4o
Distance North (km)
-20
-25
-30
-35
-40
-65
-60
-55
-50
-45
Distance East (km)

Figure 6(b)

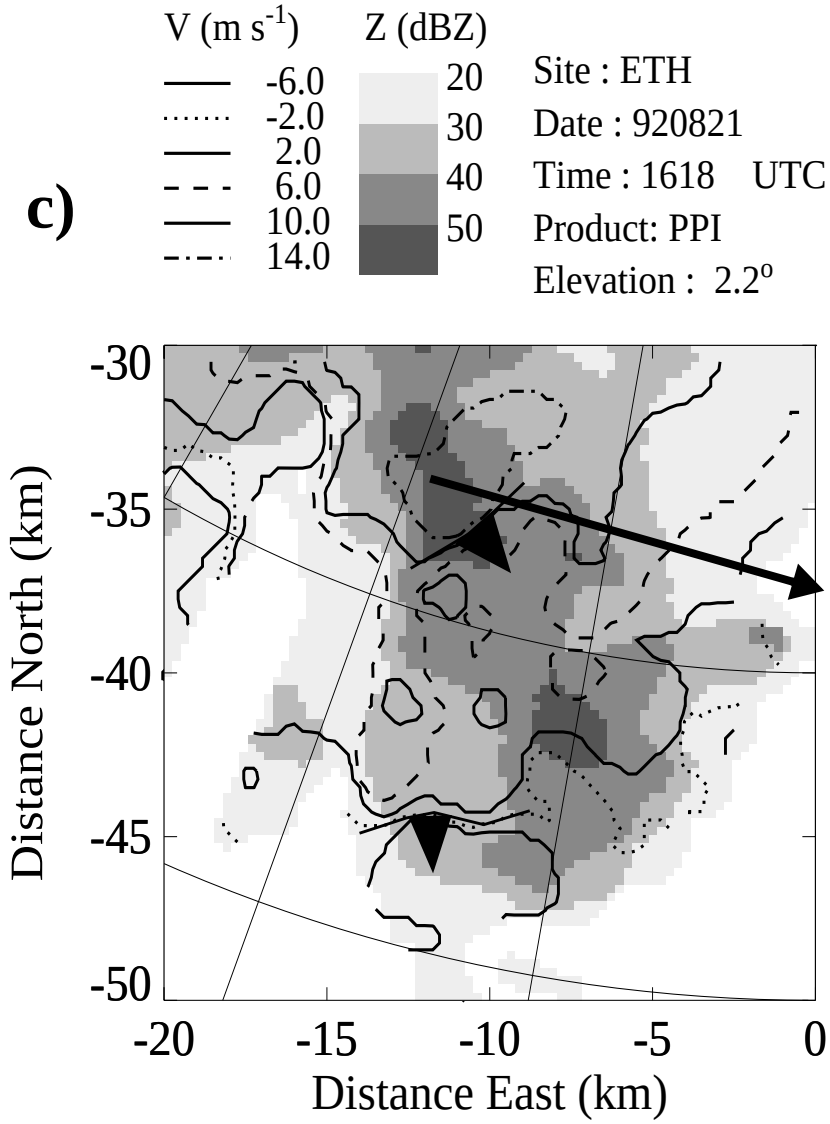
c)
V (m s-1)
-6.0
-2.0
2.0
6.0
10.0
14.0
Z (dBZ)
20
30
40
50
Site : ETH
Date : 920821
Time : 1618 UTC
Product: PPI
Elevation : 2.2o
Distance North (km)
-30
-35
-40
-45
-50
-20
-15
-10
-5
0
Distance East (km)

Figure 6(c)

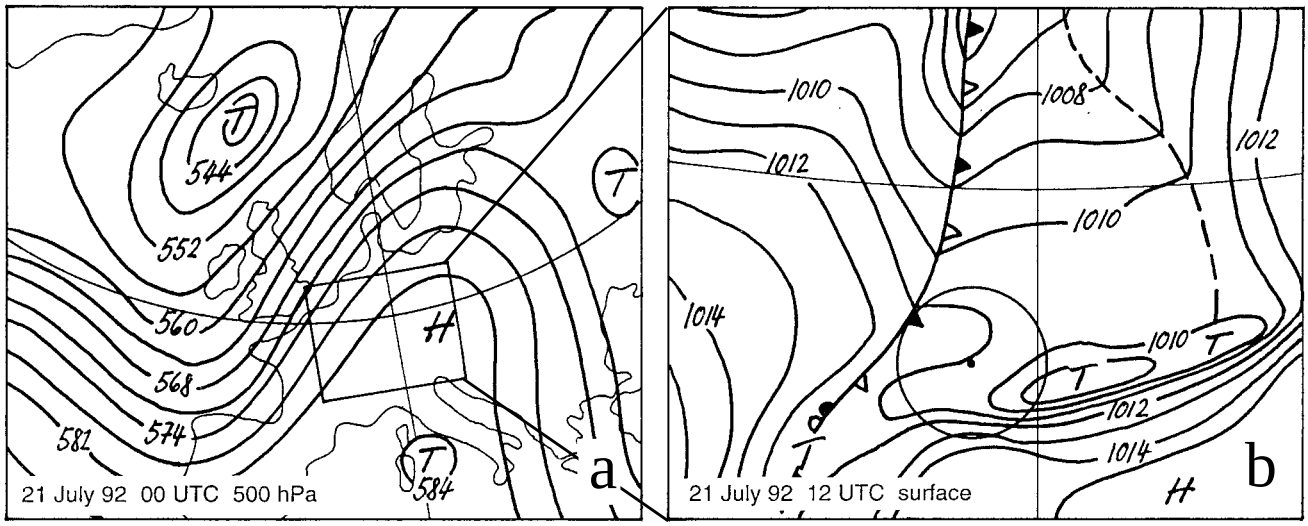
544
552
560
568
574
582
584
a
21 July 92 00 UTC 500 hPa
1010
1012
1008
1012
1010
1014
1010
1012
1014
b
21 July 92 12 UTC surface

Figure 7(a,b)

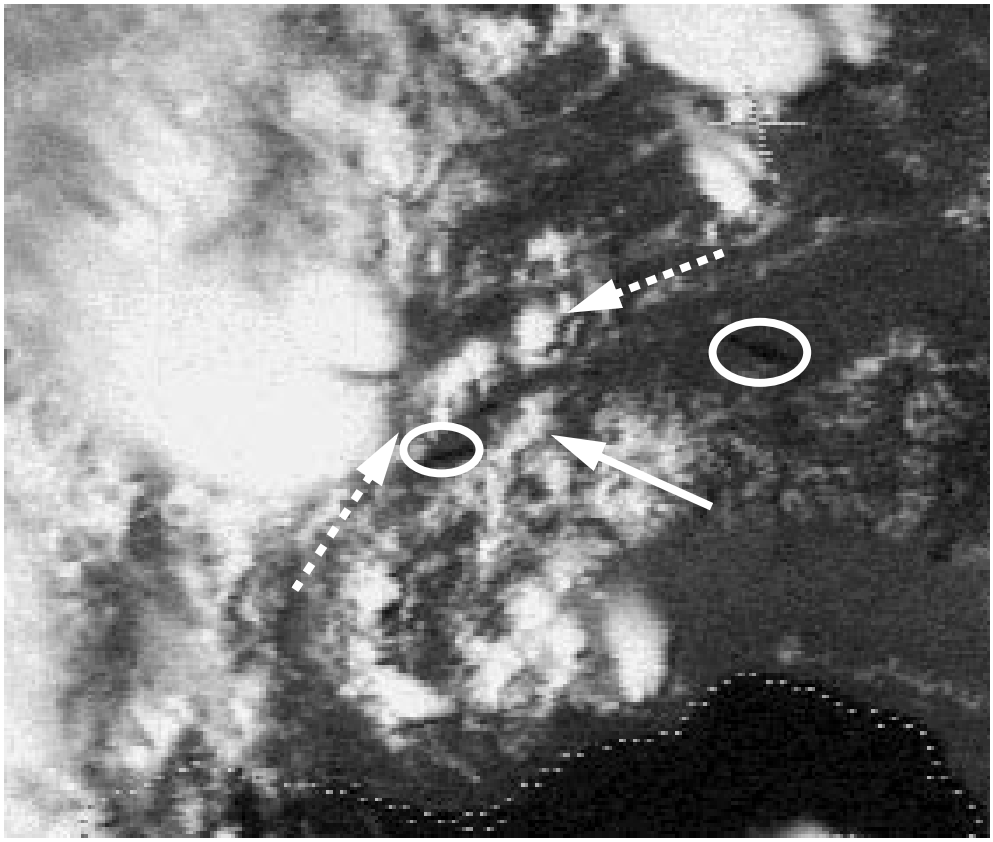

Figure 8

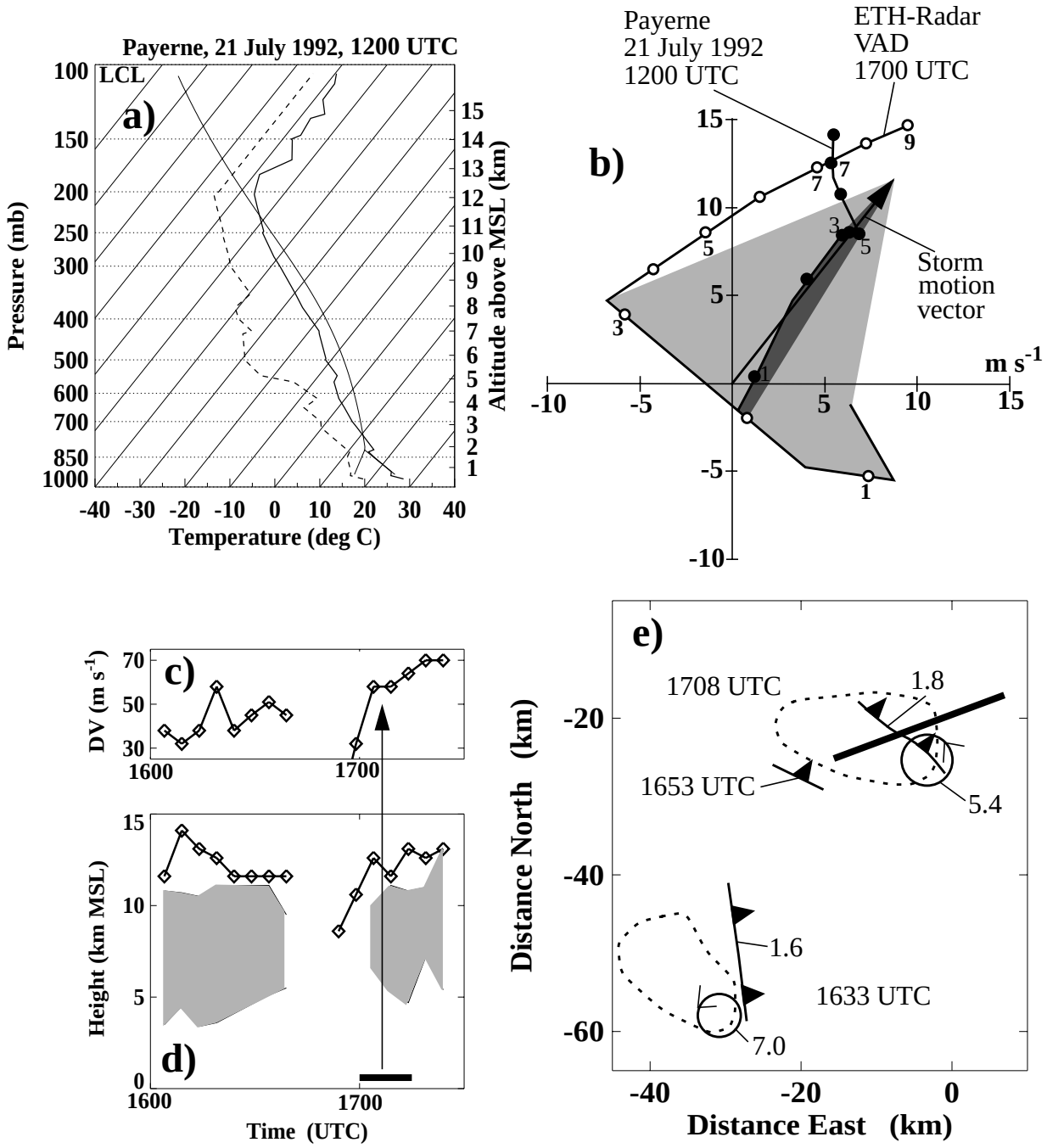

Figure 9(a,b,c,d,e)

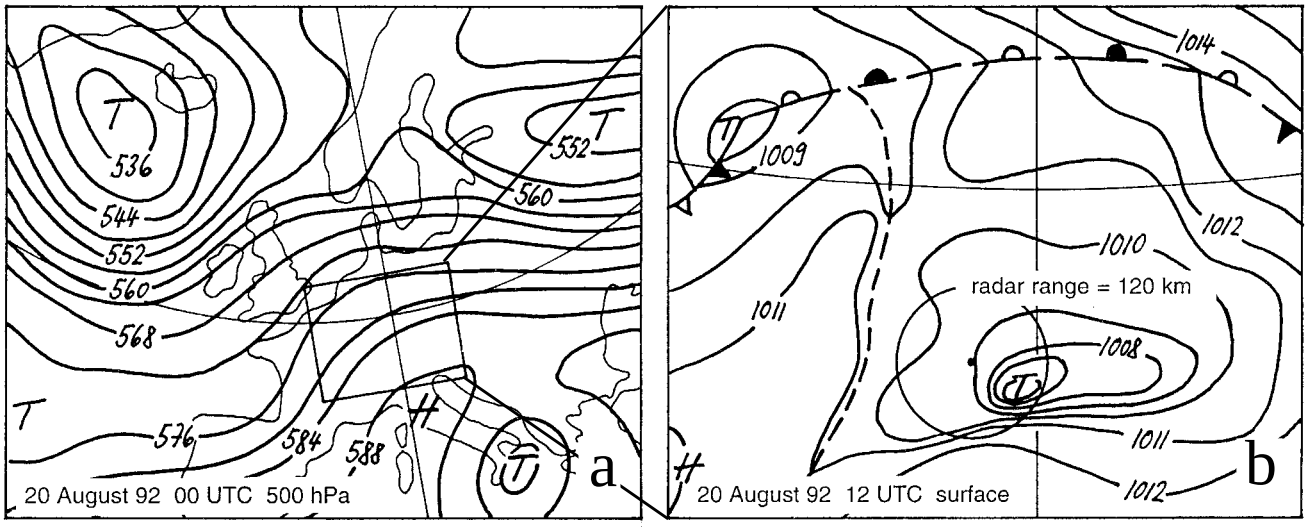
536
544
552
560
568
576
584
588
552
560
20 August 92 00 UTC 500 hPa
a
1009
1010
1011
1012
1014
radar range = 120 km
1008
1011
1012
20 August 92 12 UTC surface
b

Figure 10(a,b)

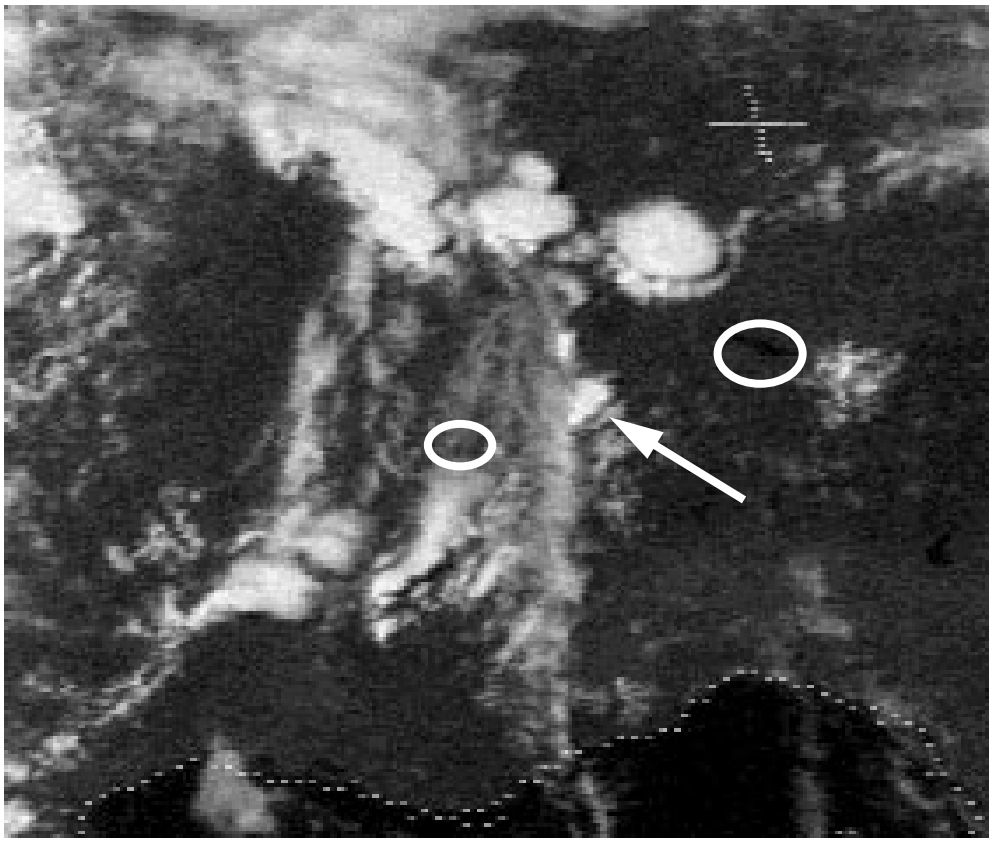

Figure 11

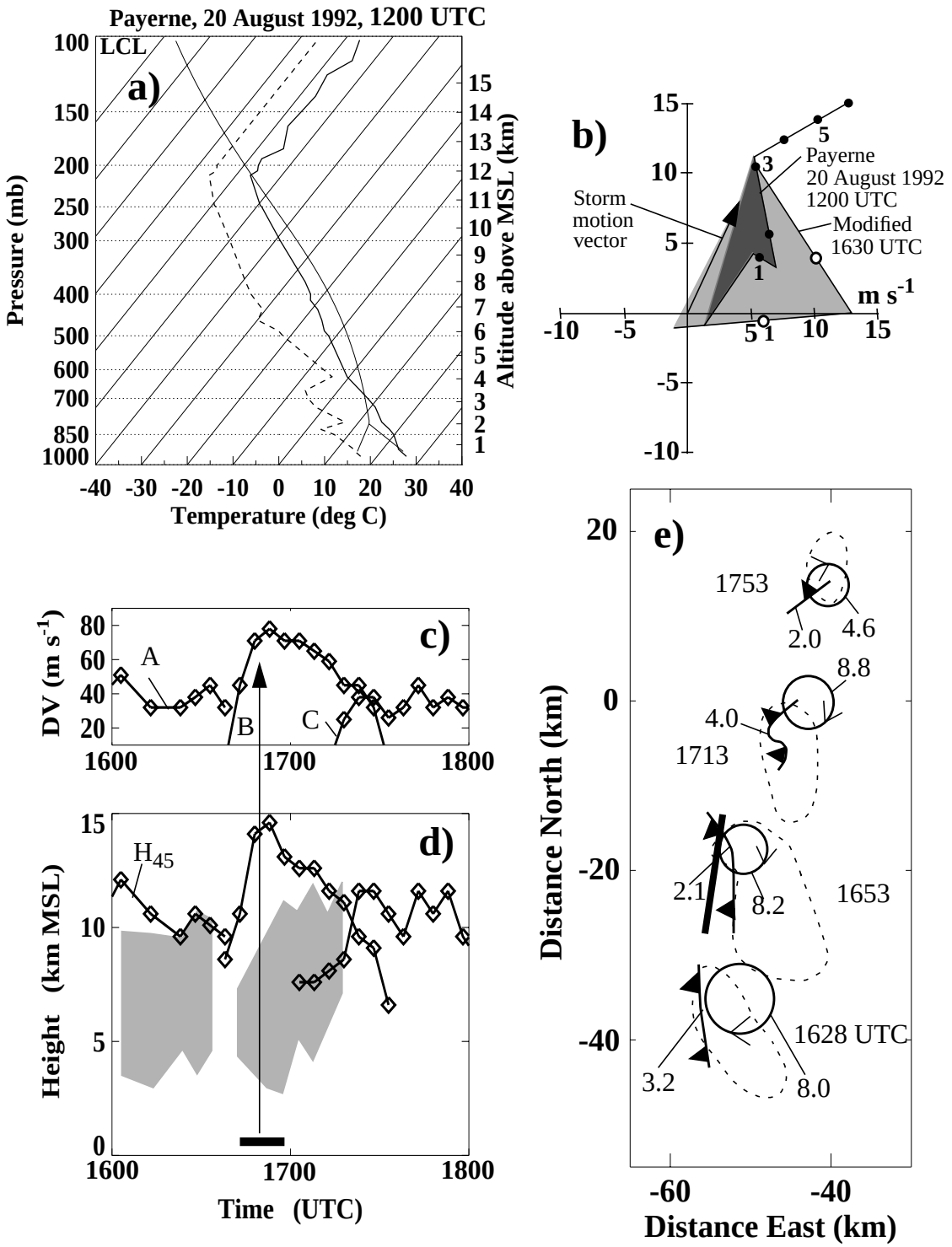

Figure 12(a,b,c,d,e)

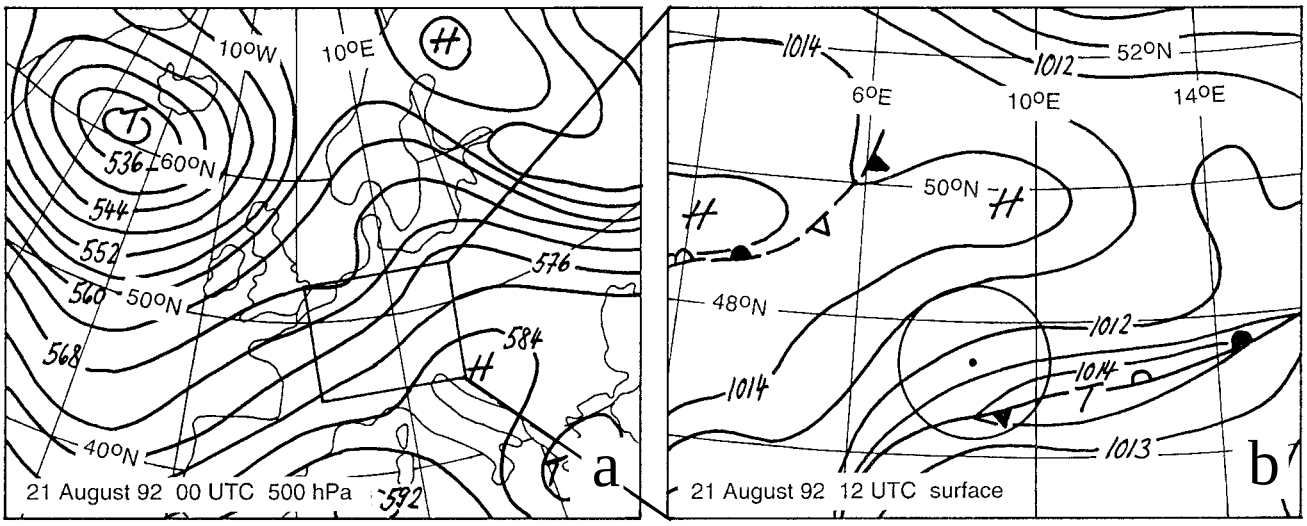
100°W
10°E
536
544
552
560
568
576
584
592
60°N
50°N
40°N
21 August 92 00 UTC 500 hPa
a
1014
1012
52°N
6°E
10°E
14°E
50°N
48°N
1012
1014
1013
21 August 92 12 UTC surface
b

Figure 13(a,b)

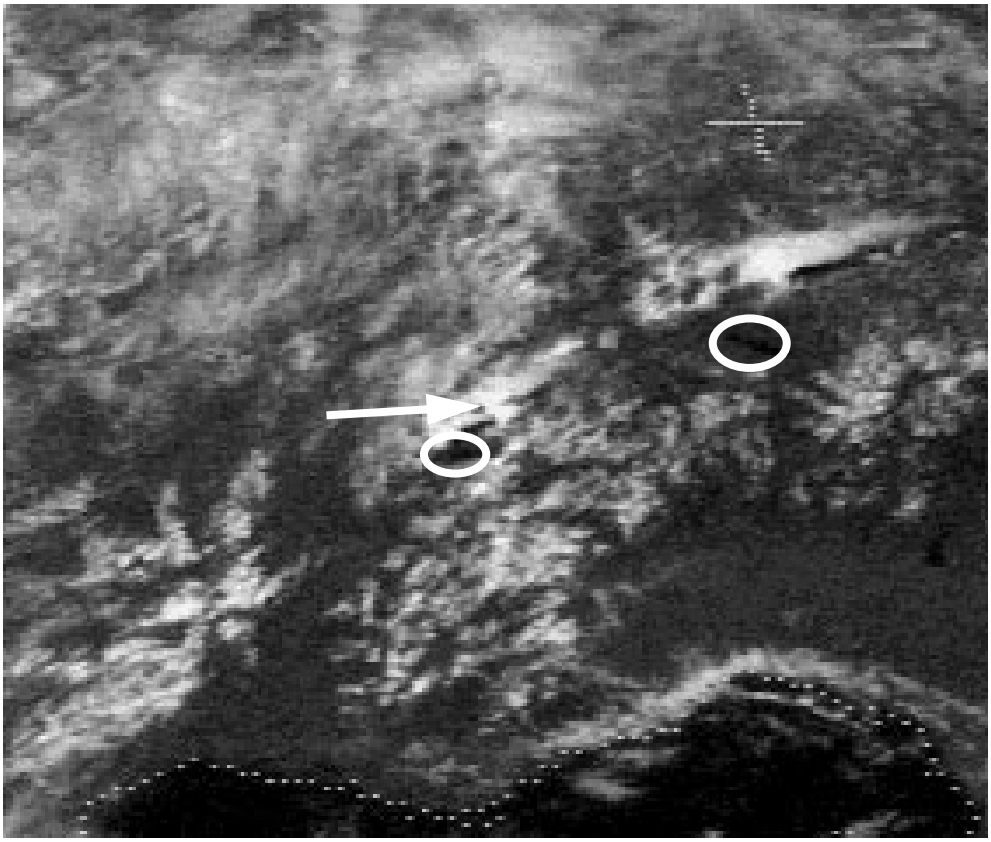

Figure 14

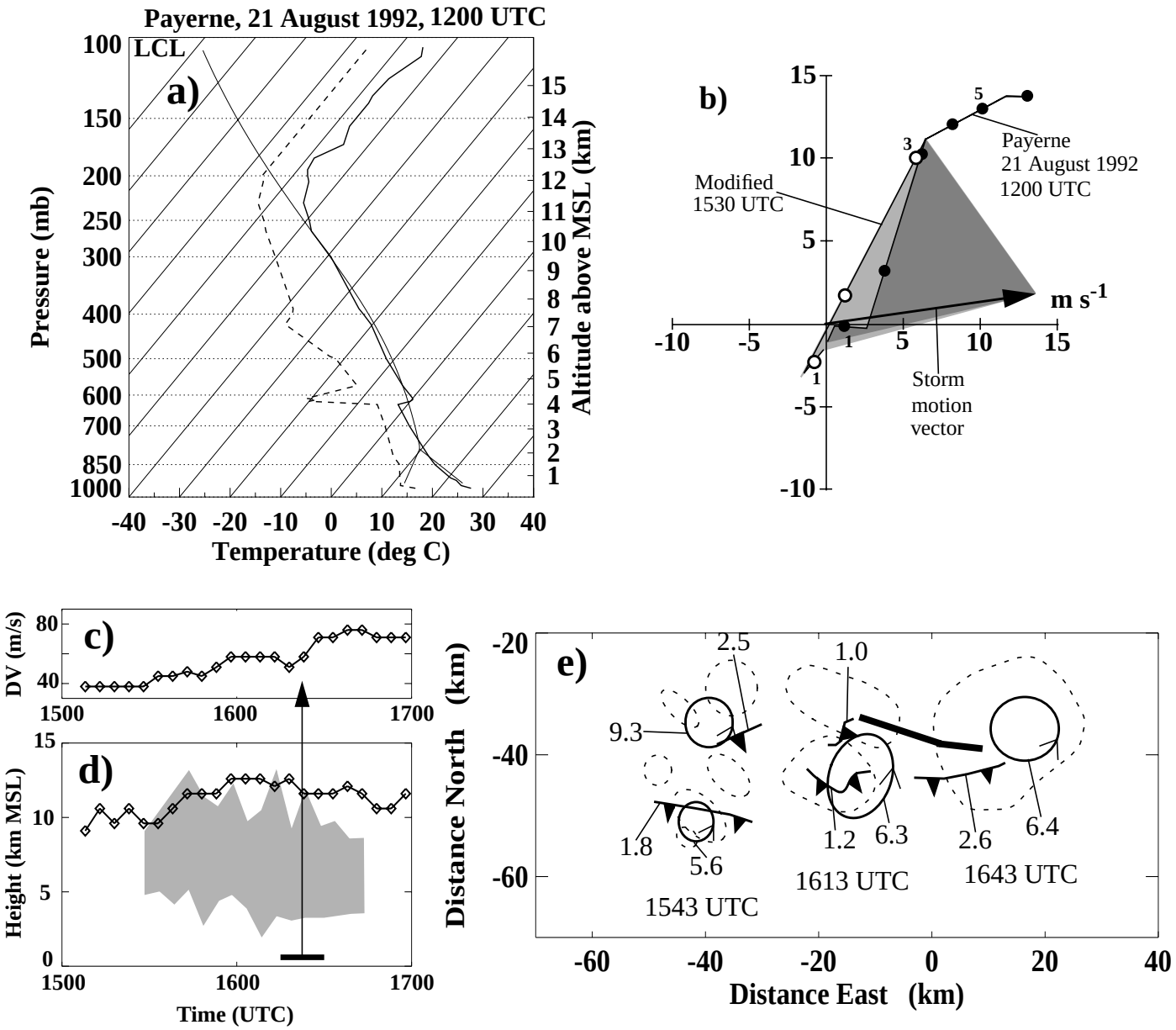

Figure 15(a,b,c,d,e)